

INFORMATION TO USERS

This reproduction was made from a copy of a document sent to us for microfilming. While the most advanced technology has been used to photograph and reproduce this document, the quality of the reproduction is heavily dependent upon the quality of the material submitted.

The following explanation of techniques is provided to help clarify markings or notations which may appear on this reproduction.

1. The sign or "target" for pages apparently lacking from the document photographed is "Missing Page(s)". If it was possible to obtain the missing page(s) or section, they are spliced into the film along with adjacent pages. This may have necessitated cutting through an image and duplicating adjacent pages to assure complete continuity.
2. When an image on the film is obliterated with a round black mark, it is an indication of either blurred copy because of movement during exposure, duplicate copy, or copyrighted materials that should not have been filmed. For blurred pages, a good image of the page can be found in the adjacent frame. If copyrighted materials were deleted, a target note will appear listing the pages in the adjacent frame.
3. When a map, drawing or chart, etc., is part of the material being photographed, a definite method of "sectioning" the material has been followed. It is customary to begin filming at the upper left hand corner of a large sheet and to continue from left to right in equal sections with small overlaps. If necessary, sectioning is continued again—beginning below the first row and continuing on until complete.
4. For illustrations that cannot be satisfactorily reproduced by xerographic means, photographic prints can be purchased at additional cost and inserted into your xerographic copy. These prints are available upon request from the Dissertations Customer Services Department.
5. Some pages in any document may have indistinct print. In all cases the best available copy has been filmed.

**University
Microfilms
International**

300 N. Zeeb Road
Ann Arbor, MI 48106

8227370

Sritharan, Sivaguru Sornalingam

NONLINEAR AERODYNAMICS OF CONICAL DELTA WINGS

The University of Arizona

PH.D. 1982

**University
Microfilms
International** 300 N. Zeeb Road, Ann Arbor, MI 48106

PLEASE NOTE:

In all cases this material has been filmed in the best possible way from the available copy. Problems encountered with this document have been identified here with a check mark .

1. Glossy photographs or pages _____
2. Colored illustrations, paper or print _____
3. Photographs with dark background _____
4. Illustrations are poor copy _____
5. Pages with black marks, not original copy _____
6. Print shows through as there is text on both sides of page _____
7. Indistinct, broken or small print on several pages _____
8. Print exceeds margin requirements _____
9. Tightly bound copy with print lost in spine _____
10. Computer printout pages with indistinct print _____
11. Page(s) _____ lacking when material received, and not available from school or author.
12. Page(s) _____ seem to be missing in numbering only as text follows.
13. Two pages numbered _____. Text follows.
14. Curling and wrinkled pages _____
15. Other _____

University
Microfilms
International

NONLINEAR AERODYNAMICS OF CONICAL DELTA WINGS

by

Sivaguru Sornalingam Sritharan

A Dissertation Submitted to the Faculty of the

PROGRAM IN APPLIED MATHEMATICS

In Partial Fulfillment of the Requirements
For the Degree of

DOCTOR OF PHILOSOPHY

In the Graduate College

THE UNIVERSITY OF ARIZONA

1 9 8 2

THE UNIVERSITY OF ARIZONA
GRADUATE COLLEGE

As members of the Final Examination Committee, we certify that we have read
the dissertation prepared by Sivaguru Sornalingam Sritharan
entitled NONLINEAR AERODYNAMICS OF CONICAL DELTA WINGS

and recommend that it be accepted as fulfilling the dissertation requirement
for the Degree of Doctor of Philosophy.

C. Richard Susan

9 August, 1982
Date

Sat Bah

9 August, 1982
Date

William R Sears

9 August 1982
Date

Alan C. Powell

9 Aug 82
Date

Lovely

Aug 10 '82
Date

Final approval and acceptance of this dissertation is contingent upon the
candidate's submission of the final copy of the dissertation to the Graduate
College.

I hereby certify that I have read this dissertation prepared under my
direction and recommend that it be accepted as fulfilling the dissertation
requirement.

C. Richard Susan
Dissertation Director

August 9, 1982
Date

STATEMENT BY AUTHOR

This dissertation has been submitted in partial fulfillment of requirements for an advanced degree at The University of Arizona and is deposited in the University Library to be made available to borrowers under rules of the Library.

Brief quotations from this dissertation are allowable without special permission, provided that accurate acknowledgement of source is made. Requests for permission for extended quotation from or reproduction of this manuscript in whole or in part may be granted by the Head of the major department or the Dean of the Graduate college when in his judgment the proposed use of the material is in the interests of scholarship. In all other instances, however, permission must be obtained from the author.

SIGNED: S. S. Srinitharan

TO MY MOTHER

ACKNOWLEDGEMENTS

The author wishes to express his deep gratitude and appreciation to Professor A.R. Seebass, Chairman of his committee, for his invaluable guidance and counsel during the course of this work. The author also would like to thank the other members of his committee, especially to Professors W.R. Sears and David Lovelock for many helpful suggestions. Drs. Manuel Salas of NASA Langley Research Center, Djordje Dulikravich of NASA Lewis Research Center and K-Y Fung of The University of Arizona are thanked for many stimulating discussions. Howard Nebeck is especially thanked for helping the author to learn the computer and being a very friendly colleague. Other students in the CFD program including Dave Kopriva, Stazek Pryzbytkowski and Shen Liang are thanked for being very exciting colleagues. Finally, Miss Linda Harper is thanked for her skillful typing of this thesis.

TABLE OF CONTENTS

	Page
LIST OF FIGURES.	vi
ABSTRACT	x
1. INTRODUCTION	1
2. IRROTATIONAL CONICAL FLOWS	5
2.1 Governing Equations	5
2.2 Some Aspects of the Cross-Flow Sonic Surface.	12
3. THE NUMERICAL METHOD	18
3.1 The finite Area Method.	18
3.2 Boundary Conditions	25
3.2.1 Outer Boundary	25
3.2.2 Symmetry Plane	25
3.2.3 Cone Surface	25
3.3 Artificial Viscosity and Upwind Differencing.	27
3.4 Construction and Analysis of the Iterative Scheme	30
3.5 Grid Generation	41
4. A DESIGN METHOD TO OBTAIN CONICAL WINGS WITH SHOCK-FREE CROSS-FLOW.	45
5. RESULTS AND DISCUSSION	51
6. CONCLUSIONS.	84
REFERENCES	86

LIST OF FIGURES

Figure		Page
1	Conical flow particle trajectories and stream surface (from Ref. 1), and sketch of flow about an elliptic cone showing bow shock wave, cross-flow sonic surface and cross-flow shock waves	2
2	Cross-flow pattern for an elliptic cone at angle of attack showing cross-flow supersonic zones, shock waves and cross-flow streamlines	9
3	Types of sonic lines that terminate on the body	15
4	The computational domain and a sketch of the bilinear parametric transformation on a unit sphere	20
5	Sketch of primary cells and the flux cell.	23
6	Flux cell arrangements at the body	26
7	Unsteady characteristic cones for subsonic and supersonic points.	40
8	Regions Ω_1 and Ω_2 are calculated respectively by the usual algorithm and the marching algorithm	49
9	Computational boundaries and various possibilities for line relaxation.	52
10a	The 16 x 16 mesh for a circular cone of 10° half angle, at 10° angle of attack	55
10b	Bow shock position for a circular cone at 10° angle of attack with $M_\infty = 2.0$. Comparison is with the rotational calculations of Jones ²²	56

Figure		Page
10c	Surface pressure distribution for a circular cone at 10° angle of attack with $M_\infty = 2.0$. Comparison is with the rotational calculations of Jones ²²	57
11a	The 32 x 32 mesh for a circular cone of 10° half angle at 10° angle of attack.	58
11b	Bow shock position for a circular cone at 10° angle of attack calculated using 32 x 32 mesh. Comparison is with the rotational calculations of Jones ²²	59
11c	Surface pressure distribution of a circular cone at 10° angle of attack at Mach 2, calculated using the 32 x 32 mesh. Comparison is with the rotational calculations of Jones ²²	60
12a	The 64 x 64 mesh for a circular cone of 10° half angle at 10° angle of attack.	61
12b	Surface distribution for a circular cone at 10° angle of attack with $M_\infty = 2.0$; 64 x 64 grid. Comparison is with the rotational calculations of Jones ²²	62
12c	Bow shock position for a circular cone of 10° half angle at 10° angle of attack. Calculated using a 64 x 64 grid. Comparison is with the rotational calculations of Jones ²²	63
12d	Pressure variation between the bow shock wave and the body for a circular cone of 10° half angle at 10° angle of attack with $M_\infty = 2.0$. Comparison is with the rotational calculations of Jones ²²	64
12e	Comparisons of the streamline patterns on a circular cone at a) 20° and b) 10° angle of attack with $M_\infty = 2.0$. Note the lift-off of the leeward node as well as the formation of a supersonic zone in the cross flow	65

Figure		Page
13a	The 16 x 16 mesh for a 6:1 elliptic cone at 10° angle of attack.	66
13b	Surface pressure distribution for a 6:1 elliptic cone at 10° angle of attack with $M_\infty = 1.97$ obtained with the 16 x 16 mesh.	67
13c	Pressure variation between the body and the bow shock wave for 6:1 elliptic cone obtained with the 16 x 16 mesh	68
14a	The 32 x 32 mesh for a 6:1 elliptic cone at 10° angle of attack	69
14b	Pressure variation between the body and the bow shock wave for a 6:1 elliptic cone at 10° angle of attack with $M_\infty = 1.97$ obtained with the 32 x 32 mesh.	70
14c	Surface pressure distribution for a 6:1 elliptic cone at 10° angle of attack with $M_\infty = 1.97$ obtained with the 32 x 32 mesh	71
15a	The 64 x 64 mesh for a 6:1 elliptic cone at 10° angle of attack	72
15b	Pressure variation between the body and the shock wave for the elliptic cone at 10° angle of attack with $M_\infty = 1.97$ obtained with a 64 x 64 mesh	73
15c	Bow shock position and the cross-flow sonic surface for the 6:1 elliptic cone at 10° angle of attack with $M_\infty = 1.97$ obtained with a 64 x 64 mesh	74
15d	Comparison of the surface pressures using the Euler equations due to Siclari ²³ with the present results for a 6:1 elliptic cone at 10° angle of attack with $M_\infty = 1.97$	75
16a	The 64 x 64 mesh for a 13:1 elliptic cone at 10° angle of attack.	76

Figure	Page
16b	Bow shock position and the cross-flow sonic surface for a 13:1 elliptic cone at 10° angle of attack 77
16c	Pressure variation between the bow shock wave and the body for a 13:1 elliptic cone at 10° angle of attack at $M_\infty = 2.0$ 78
16d	Comparison of the surface pressure using the Euler equation due to Siclari ²³ and a quasilinear formulation of the potential equation due to Grossman ¹⁸ with the present result for a 13:1 elliptic cone at 10° angle of attack with $M_\infty = 2.0$ 79
17a	Bow shock position and the cross-flow sonic surface for a 10° circular cone at 20° angle of attack with $M_\infty = 2.0$ 80
17b	Bow shock position and the smooth sonic surface obtained by changing the gas law inside the sonic bubble for a 10° circular cone at 20° angle of attack with $M_\infty = 2.0$ 81
17c	Surface pressure distribution of a 10° circular cone at 20° angle of attack with $M_\infty = 2.0$ 82
17d	Surface pressure distribution on the circular cone modified to provide a shock-free cross-flow. 83

ABSTRACT

Steady, inviscid, supersonic flow past conical wings is studied within the context of irrotational, nonlinear theory. An efficient numerical method is developed to calculate cones of arbitrary section at incidence. The method is fully conservative and implements a body conforming mesh generator. The conical potential is assumed to have its best linear variation inside each cell; a secondary interlocking cell system is used to establish the flux balance required to conserve mass. In regions of supersonic cross flow, the discretization scheme is desymmetrized by adding the appropriate artificial viscosity in conservation form. The algorithm is nearly an order of magnitude faster than present Euler methods. It predicts known results as long as the flow Mach numbers normal to the shock waves are near 1; qualitative features, such as nodal point lift-off, are also predicted correctly. Results for circular and thin elliptic cones are shown to compare very well with calculations using Euler equations. This algorithm is then implemented in the design of conical wings to be free from shock waves terminating embedded supersonic zones adjacent to the body. This is accomplished by generating a smooth cross-flow sonic surface by using a fictitious gas law that makes the governing equation elliptic inside the cross-flow sonic surface. The shape of the wing required to provide this shock-free flow, if such a flow is consistent with the sonic surface data, is found by solving the Cauchy problem inside the sonic

surface using the data on this surface and, of course, the correct gas law. This design procedure is then demonstrated using the simple case of a circular cone at angle of attack.

CHAPTER 1

INTRODUCTION

Conical flows are one of the simplest types of inviscid flows that have the basic features of a three-dimensional flow. A flow field is classified as conical when all the physical properties, namely, viz., the pressure, density, velocity and entropy, remain constant along every straight line through a given point called the apex. Conical flow is found to exist, for example, around cones of finite length in supersonic flow because of the Law of Forgiven Signals¹. Topological features of conical flows can be easily understood by studying the cross-flow streamlines, that is, the traces of the conical stream surfaces's intersection with a sphere, as sketched in Figure 1. The cross-flow streamlines will have critical points where the cross-flow velocities vanish. For a special class of critical points, one can derive rules for the number of these points using Poincare indices. Thus, for example, irrotational conical flows will have an equal number of saddle points and nodes. At high angle of attack, conical streamline patterns exhibit certain global changes such as the lift off of the leeward node and, perhaps, the appearance of spiral nodes. In addition, the cross flow may become supersonic as it expands about the leading edge, leading to an embedded supersonic cross-flow region terminated by a shock wave. The isentropic assumption retains all of the topological features of

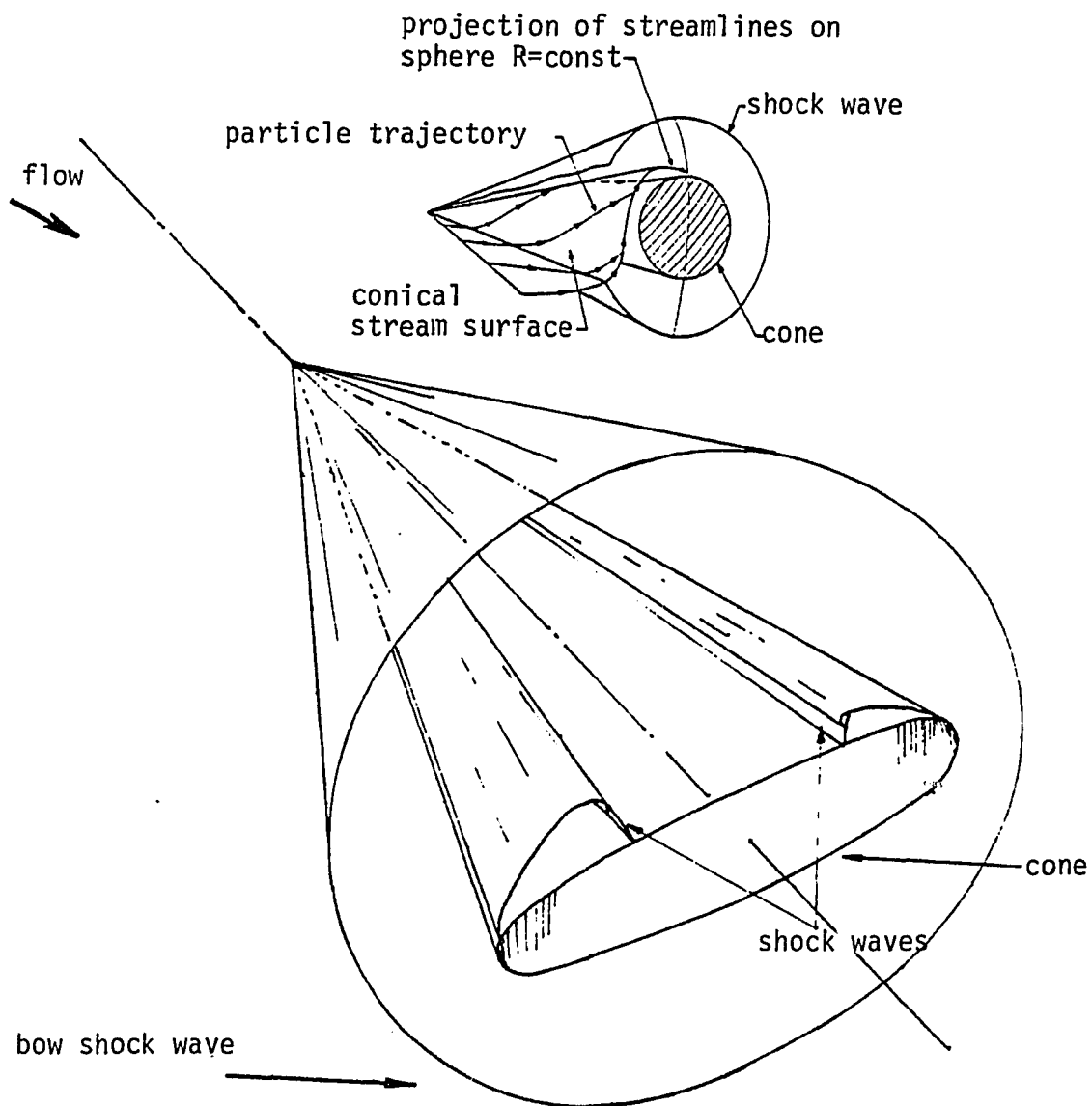


Figure 1. Conical flow particle trajectories and stream surface (from Ref. 1), and sketch of flow about an elliptic cone showing bow shock wave, cross-flow sonic surface and cross-flow shock waves.

these flows except spiral nodes² and should provide an adequate approximation to the quantitative flow features if the normal Mach number to any shock is less than 1.2³. This approximation greatly simplifies the computations because the governing equation is scalar and the multivalued possibility at the nodal point (vortical singularity) is eliminated.

It is well known that the most suitable flow structure for a classical slender-wing airplane has leading-edge separation. The resulting vortices are highly stable and, while contributing to the induced drag, also increase the lift because of the low pressures they induce. These vortices usually increase the lift-to-drag ratio for a delta wing. In fact, all the slender-wing configurations have this kind of flow structure. However, the modern supercruiser concept demands efficient supersonic cruise and high-level transonic, as well as supersonic, maneuverability⁴. In order to obtain this level of performance, the wings have to be relatively thick, should have transonic leading edges and attached flow⁵. A delta wing with transonic leading edge will, in general, have cross-flow shocks. To obtain attached flow this configuration should have a cross flow that is shock free or contains only weak shocks.

A recent assessment of the existing aerodynamic design techniques for supersonic aircraft⁶ shows that there is need for a numerical method that is reliable, reasonably fast and, most important of all, can handle arbitrary geometries. The present study was tailored to meet these needs to some extent, but is restricted to conical wings.

In this thesis, the theory of irrotational conical flows is described in a general coordinate system defined on a unit sphere. A finite area method is described⁷ that represents an extension of Jameson's finite volume method⁸ to vector fields defined on a curved surface. The local similarity between the highest-order terms of the partial differential equation describing conical flows and that describing plane transonic flows has been exploited to devise a suitable artificial viscosity to implement the entropy condition, as well as to construct a stable iteration scheme. In the second part of the thesis, a method is described for finding cones with shock-free cross flow.

CHAPTER 2

IRROTATIONAL CONICAL FLOWS

2.1 Governing Equations

We may obtain the equations governing conical flow in a general coordinate system by first projecting the Euler equations for a general three-dimensional flow onto a sphere of radius r , and then scaling them to obtain the description on the unit sphere. For the irrotational formulation we only need the mass continuity and the energy equations. We first note that the mainstream velocity components, Q^i , and their projection on the sphere of radius r , \tilde{V}^α , are related by

$$\tilde{V}^\alpha = B_i^\alpha Q^i,$$

where

$$B_\alpha^i = \frac{\partial X^i}{\partial \Xi^\alpha}, \quad \alpha = 1, 2 \text{ and } i = 1, 2, 3$$

are the projection factors (or the tangent vectors). Here, X^i are coordinates in Euclidian 3-space and Ξ^α are the parametric coordinates on the surface of the sphere. Thus, the magnitude of mainstream velocity

$$Q^2 = Q^i Q_i = \tilde{V}^\alpha \tilde{V}_\alpha + Q_R^2$$

where Q_R is the radial velocity. Therefore, the mainstream flux vector, L^i , and the cross-flow flux vector, \tilde{W}^α , (both are relative tensors⁹ of type 1-0-1 in their respective spaces) are related by

$$\tilde{W}^\alpha = B_i^\alpha L^i,$$

where

$$\tilde{W}^\alpha = \rho \sqrt{\tilde{g}} \tilde{V}^\alpha$$

and

$$L^i = \rho \sqrt{G} Q^i$$

Here, ρ is the gas density, G and \tilde{g} are respectively the determinants of the metric tensors in spaces x^i and Ξ^α .

Now if we choose the same coordinates, Ξ^α , on the unit sphere with metric tensor $g_{\alpha\beta}$, then

$$g_{\alpha\beta} = \frac{1}{r^2} \tilde{g}_{\alpha\beta}, \quad g^{\alpha\beta} = r^2 g^{\alpha\beta}$$

and if we choose x^i as (Ξ^1, Ξ^2, r) then,

$$g = \frac{1}{r^4} \tilde{g} = \frac{1}{r^4} G.$$

If we note that the magnitude of cross-flow velocity

$$q_c^2 = \tilde{V}^\alpha \tilde{V}_\alpha = V^\alpha V_\alpha$$

is independent of r , where V^α is the velocity defined on the unit sphere, we get the relations

$$V_\alpha = \frac{1}{r} \tilde{V}_\alpha \quad \text{and} \quad V^\alpha = r \tilde{V}^\alpha.$$

Thus, the flux vector on the unit sphere $W^\alpha = \rho \sqrt{g} V^\alpha$ is related to the mainstream flux vector by

$$W^\alpha = \frac{1}{r} L^i B_i^\alpha.$$

If we now consider the divergence for the relative tensor W^α , then

$$W^\alpha \parallel_\alpha = \frac{\partial W^\alpha}{\partial \Xi^\alpha}$$

$$\begin{aligned}
&= \frac{\partial}{\partial \Xi^\alpha} \left[\frac{1}{r} L^i B_i^\alpha \right] \\
&= \frac{1}{r} \frac{\partial L^i}{\partial x^j} B_\alpha^j B_i^\alpha + \frac{1}{r} L^i \frac{\partial}{\partial \Xi^\alpha} B_i^\alpha \\
&= \frac{1}{r} \frac{\partial L^i}{\partial x^j} \left[\delta_i^j - N^j N_i \right] + 0
\end{aligned}$$

Here N^i is the normal, and $B_i^\alpha = \tilde{g}^{\alpha\beta} G_{ij} B_\beta^j$.

Thus,

$$W_\alpha^\alpha \Big|_\alpha = \frac{1}{r} L^i \Big|_i - \frac{1}{r} \frac{\partial L^3}{\partial x^3}.$$

The first term in the right-hand side is the divergence for the main-stream flux and thus equal to zero. Thus, using the earlier relations, we find the continuity equation for conical flows on a unit sphere to be

$$\frac{\partial \rho \sqrt{g} V^\alpha}{\partial \Xi^\alpha} + 2\rho \sqrt{g} Q_R = 0.$$

If the irrotational assumption is made, the velocity Q^i will have a potential $\phi(x^i)$ such that, for conical flows

$$\phi(x^i) = rF(\Xi^\alpha)$$

where $F(\Xi^\alpha)$ may be called the conical potential, since

$$V_\alpha = \frac{\partial F}{\partial \Xi^\alpha} \quad \text{and} \quad Q_R = F(\Xi^\alpha).$$

For the purpose of analysis, we scale all the variables with the freestream values and thus obtain continuity of cross-flow vector field, namely, viz.,

$$\frac{\partial \rho \sqrt{g} V^\alpha}{\partial \Xi^\alpha} + 2\rho \sqrt{g} F = 0, \quad (2.1)$$

where

$$V^\alpha = g^{\alpha\beta} \frac{\partial f}{\partial \Xi^\beta} \quad , \quad (2.2)$$

and energy equation giving the density is

$$\rho^{\gamma-1} = 1 + \frac{\gamma-1}{2} M_\infty^2 (1 - V^\alpha V_\alpha - F^2) \quad . \quad (2.3)$$

Here M_∞ is the freestream Mach number and γ the specific heat ratio.

Substituting Equations (2.2) and (2.3) into Equation (2.1) and performing the differentiation, we find the quasilinear form of the governing partial differential equation:

$$\rho \sqrt{g} \left[\left(g^{\alpha\beta} - \frac{V^\alpha V^\beta}{a^2} \right) \frac{\partial^2 F}{\partial \Xi^\alpha \partial \Xi^\beta} + H \left(F, \frac{\partial F}{\partial \Xi^\alpha}, g^{\alpha\beta} \right) \right] = 0 \quad (2.4)$$

where a , the speed of sound, is given by

$$a^2 M_\infty^2 = \rho^{\gamma-1} \quad . \quad (2.5)$$

Equation (2.4) changes its type when

$$\left(g^{12} - \frac{UV}{a^2} \right)^2 - \left(g^{11} - \frac{U^2}{a^2} \right) \left(g^{22} - \frac{V^2}{a^2} \right) = 0$$

or, noting $g > 0$ always, when

$$\frac{1}{g} \left(\frac{q_c^2}{a^2} - 1 \right) = 0 \quad .$$

Here we use the notation

$$V^\alpha = \begin{pmatrix} U \\ V \end{pmatrix}, \quad V_\alpha = \begin{pmatrix} U \\ V \end{pmatrix} \quad \text{and} \quad \Xi^\alpha = \begin{pmatrix} \xi \\ \eta \end{pmatrix} .$$

Thus, the equation is hyperbolic, parabolic or elliptic depending on whether the cross-flow Mach number, M_c , is greater, equal or less than one (see Figure 2). We could also derive this result by choosing a local coordinate system aligned with the cross-flow streamlines.

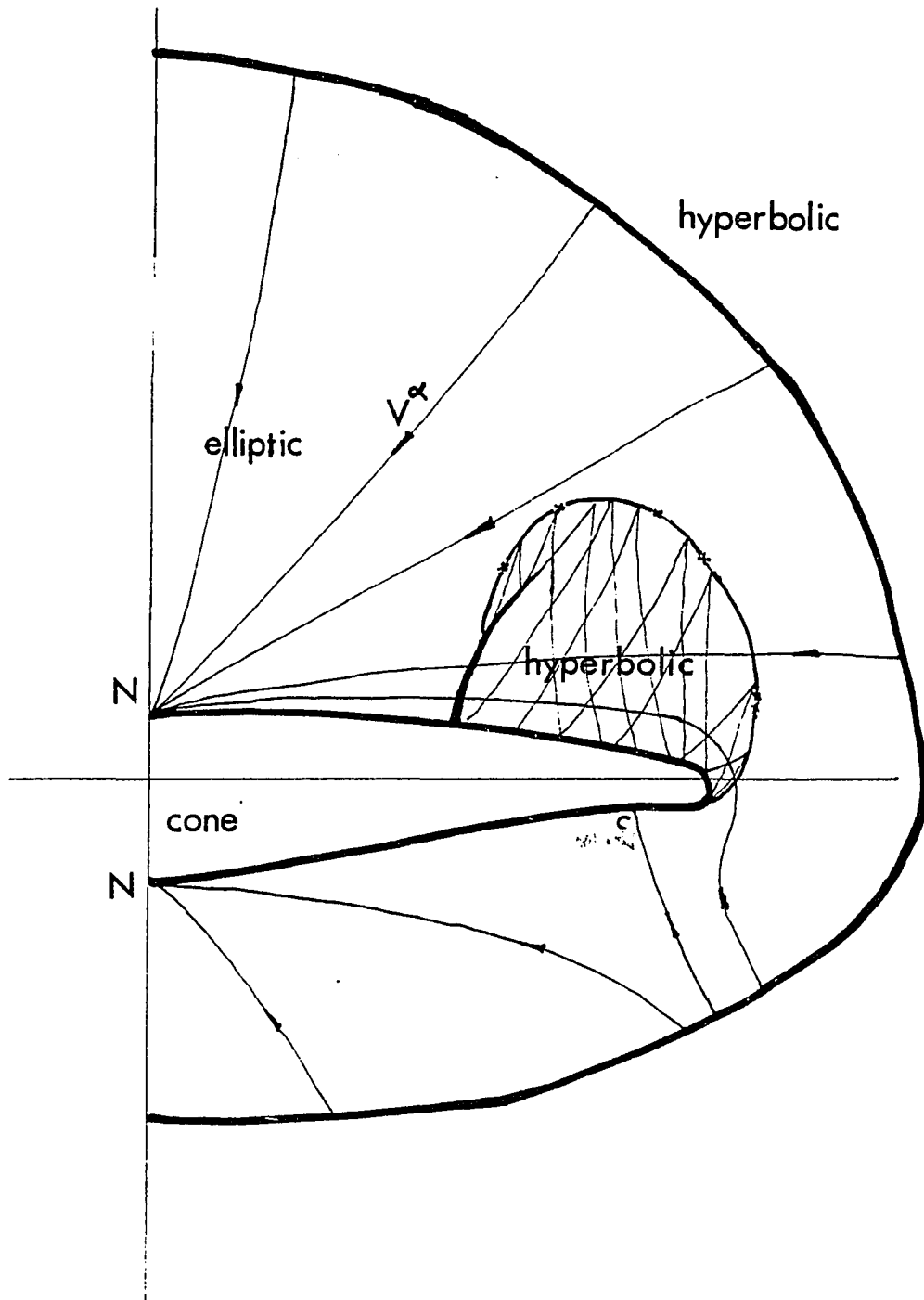


Figure 2. Cross-flow pattern for an elliptic cone at angle of attack showing cross-flow supersonic zones, shock waves and cross-flow streamlines.

We define streamwise and normal coordinates, s , n , such that

$$V_\alpha \frac{\partial \Xi^\alpha}{\partial n} = 0 \quad \text{and} \quad \epsilon_{\alpha\beta} V^\alpha \frac{\partial \Xi^\beta}{\partial s} = 0$$

$$\text{with } g_{\alpha\beta} \frac{\partial \Xi^\alpha}{\partial n} \frac{\partial \Xi^\beta}{\partial n} = g_{\alpha\beta} \frac{\partial \Xi^\alpha}{\partial s} \frac{\partial \Xi^\beta}{\partial s} = 1 \quad .$$

Here $\epsilon_{\alpha\beta}$ is the surface permutation symbol. Then we find

$$\frac{\partial \Xi^\alpha}{\partial s} = \frac{V^\alpha}{q_c} \quad , \quad \frac{\partial \xi}{\partial n} = -\frac{1}{\sqrt{g}} \frac{v}{q_c} \quad \text{and} \quad \frac{\partial \eta}{\partial n} = \frac{1}{\sqrt{g}} \frac{u}{q_c} \quad .$$

Note also that in these coordinates

$$\frac{\partial F}{\partial s} = \frac{\partial F}{\partial \Xi^\alpha} \frac{\partial \Xi^\alpha}{\partial s} = \frac{V_\alpha V^\alpha}{q_c} = q_c$$

and

$$\frac{\partial F}{\partial n} = \frac{\partial F}{\partial \xi} \left(-\frac{1}{\sqrt{g}} \frac{v}{q_c} \right) + \frac{\partial F}{\partial \eta} \left(\frac{1}{\sqrt{g}} \frac{u}{q_c} \right) = 0 \quad .$$

Similarly, we also obtain the relations

$$\frac{\partial^2 F}{\partial s^2} = \frac{V^\alpha V^\beta}{q_c^2} \frac{\partial^2 F}{\partial \Xi^\alpha \partial \Xi^\beta} + \dots \quad ,$$

and

$$\frac{\partial^2 F}{\partial n^2} = \left(g^{\alpha\beta} - \frac{V^\alpha V^\beta}{q_c^2} \right) \frac{\partial^2 F}{\partial \Xi^\alpha \partial \Xi^\beta} + \dots \quad .$$

Using these relations, we may write the governing partial differential equation as

$$-\rho \frac{\sqrt{g}}{a^2} \left[(q_c^2 - a^2) \frac{\partial^2 F}{\partial s^2} - a^2 \frac{\partial^2 F}{\partial n^2} \right] + \dots = 0 \quad (2.6)$$

We also note the following structure of these equations. Replacing the expression for $\partial^2 F / \partial s^2$, we obtain

$$-\frac{\rho\sqrt{g}}{a^2} \left[\mu V^\alpha V^\beta \frac{\partial^2 F}{\partial \Xi^\alpha \partial \Xi^\beta} - a^2 \frac{\partial^2 F}{\partial n^2} \right] + \dots = 0$$

where

$$\mu = \left(1 - \frac{a^2}{q_c^2} \right) .$$

Now, if we define two functions \tilde{P} , \tilde{Q} such that

$$\tilde{P} = \mu\rho \frac{\sqrt{g}}{a^2} \left(U^2 \frac{\partial^2 F}{\partial \xi^2} + UV \frac{\partial^2 F}{\partial \xi \partial \eta} \right)$$

and

$$\tilde{Q} = \mu\rho \frac{\sqrt{g}}{a^2} \left(UV \frac{\partial^2 F}{\partial \xi \partial \eta} + V^2 \frac{\partial^2 F}{\partial \eta^2} \right) ,$$

then the partial differential equation becomes

$$-(\tilde{P} + \tilde{Q}) + \rho\sqrt{g} \frac{\partial^2 F}{\partial n^2} + \dots = 0 . \quad (2.7)$$

This form is useful for explaining the introduction of a conservative artificial viscosity.

Finally, we note that the governing equation is of quasi-linear type and, hence, that it admits shock jumps. The jump condition that conserves mass follows immediately from Equation (2.1):

$$\left(\frac{d\eta}{d\xi} \right)_{\text{shock}} = \frac{[[\rho\sqrt{g}V]]}{[[\rho\sqrt{g}U]]} \quad (2.8)$$

where $[[\dots]]$ denotes the change in the variable across the discontinuity. The above is obviously the jump condition also implied by the mainstream continuity equation together with the conical assumption.

2.2 Some Aspects of the Cross-Flow Sonic Surface

Sonic bubbles that appear in conical cross flows differ from those of transonic flows in many aspects. In transonic flow the flow properties attain uniform state on the sonic line, whereas in conical flows the appearance of the radial velocity term in the Bernoulli equation causes the flow properties to vary along the sonic line. Plane transonic flow is governed by a homogeneous set of partial differential equations and, therefore, it is possible to obtain a linear problem through a Legendre transformation. This property also gives us the well-known Nikolskii-Taganov monotonic rule¹⁰: if an observer moves along the sonic line keeping the subsonic zone always to his left, then the stream vector will rotate in the clockwise direction. However, in conical flows, due to the inhomogeneous terms in the governing equation, it is not possible to obtain linear equations using a hodograph transformation, and also it is difficult to say anything definite about the streamline slope. Some properties of conical sonic surfaces have been worked out by Salas¹¹, and, with the aid of some of his results, we will study some relevant aspects for shock-free flows.

First, we note an interesting behavior of the pressure at the point where a cross-flow streamline exits the hyperbolic zone. Consider the Bernoulli equation

$$\frac{1}{2} (q_c^2 + F^2) + \frac{\gamma}{\gamma-1} \frac{P}{\rho} = \text{constant}; \quad (2.9)$$

taking the derivative in the s direction and substituting the adiabatic relation

$$p = \frac{1}{\gamma M_\infty^2} \rho^\gamma ,$$

we get

$$\frac{\partial p}{\partial s} = -\rho q_c \left[\frac{\partial q_c}{\partial s} + F \right] .$$

Now, from the definition of the cross-flow Mach number,

$$\frac{\partial M_c}{\partial s} = \frac{1}{a} \left[\frac{\partial q_c}{\partial s} - M_c \frac{\partial a}{\partial s} \right] .$$

Using this and the energy equations, we obtain the relation at the sonic surface for the streamwise pressure gradient, namely,

$$\frac{\partial p}{\partial s} = - \left(\frac{2}{\gamma+1} \right) \rho q_c \left[q_c \frac{\partial M_c}{\partial s} + F \right] . \quad (2.10)$$

From this we see that since F is always positive, the pressure always decreases when the streamline enters the hyperbolic zone, which is similar to transonic flows. However, when it exits the hyperbolic zone, the pressure could either increase or decrease. This is in contrast to what happens in transonic flows where the pressure always increases as the streamline exits the sonic surface because the radial velocity term F does not appear in the equation for $\frac{\partial p}{\partial s}$. This possibility leads us to believe that a shock-free situation is more likely in conical flows. We recall here that in transonic flows the shock-free situation has been proved to be mathematically isolated¹². A similar perturbation theory for shock-free conical flows does not yet exist and shock-free solutions have not previously been shown to exist.

Next, we will observe a unique feature of the cross-flow sonic line. We will first obtain a description for the sonic line by expanding the cross-flow velocity and the speed of sound and equating them. Thus, we write

$$a = a^* + \left(\frac{\partial a}{\partial s}\right)^* ds + \left(\frac{\partial a}{\partial n}\right)^* dn + \dots ,$$

$$q_c = a^* + \left(\frac{\partial q_c}{\partial s}\right)^* ds + \left(\frac{\partial q_c}{\partial n}\right)^* dn + \dots ,$$

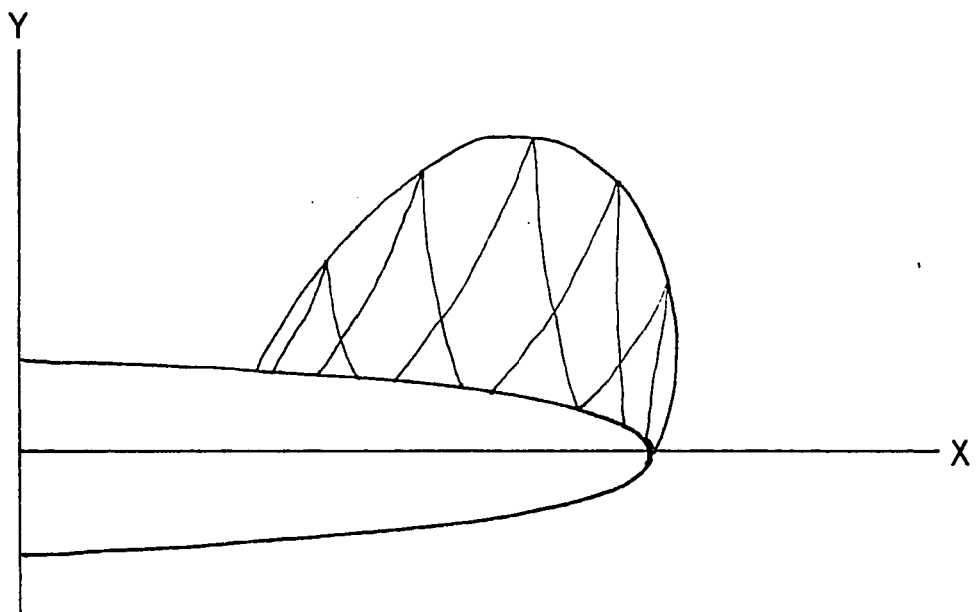
and also, from the energy equation,

$$\left(\frac{\partial a}{\partial n}\right)^* = - \left(\frac{\gamma-1}{2}\right) \left(\frac{\partial q_c}{\partial n}\right)^* .$$

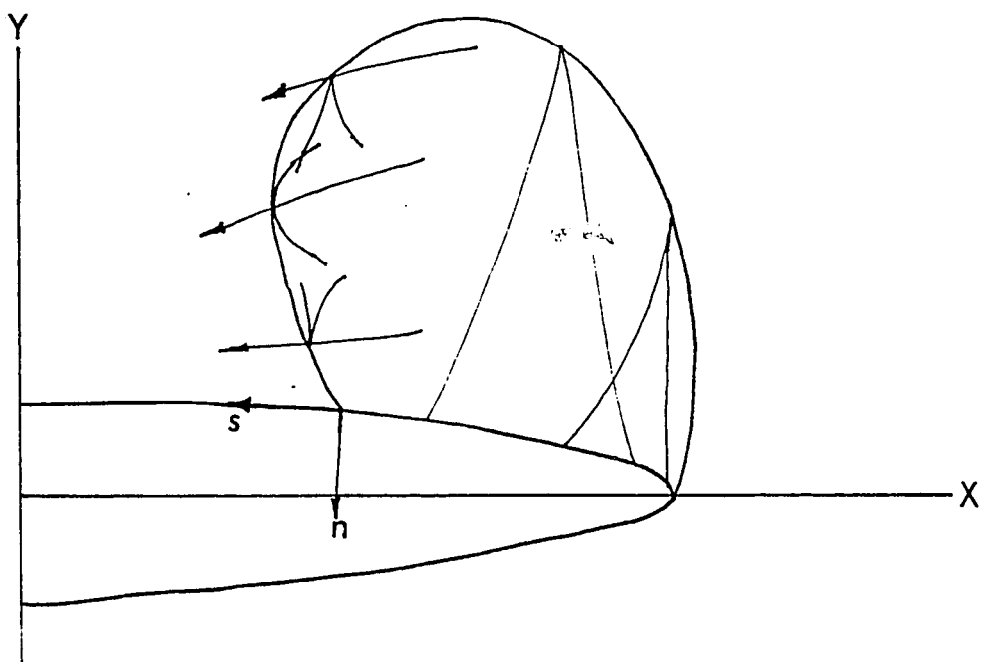
Thus, the equation of the line $q_c = a$ is

$$\left(\frac{dn}{ds}\right)_{\text{sonic line}} = - \left(\frac{2}{\gamma+1}\right) a^* \frac{\left(\frac{\partial M_c}{\partial s}\right)^*}{\left(\frac{\partial q_c}{\partial n}\right)^*} \quad (2.11)$$

This relation indicates that the angle at which the cross-flow sonic line meets the body is determined by the sign of $\left(\frac{\partial q_c}{\partial n}\right)^*$. This means that if this quantity is negative, the sonic line could meet the body at an obtuse angle. Salas incorrectly predicts this possibility for a circular cone and then uses an argument based on pressure to speculate on the possibility of a shock wave. However, one could rule out the existence of smooth flow with this kind of a bubble using the following rigorous argument. At the sonic line, the characteristics are normal to the streamlines and, therefore, from Figure 3, it is clear that for a sonic line of this kind, characteristics of the same family will intersect. Thus, if, through the



Shock free crossflow



Sonic line meeting the body at an obtuse angle

Figure 3. Types of sonic lines that terminate in the body.

above analysis, we arrive at a sonic line of this type, then for this cone a shock-free cross flow is impossible. In fact, one may work out a rule to identify conical shapes for which shock-free cross flow is impossible. For convenience, we will work in the stereographically projected plane. If one chooses a Cartesian system (x, y) in this plane, then the metric tensor will be:

$$g_{\alpha\beta} = \begin{bmatrix} J^2 & 0 \\ 0 & J^2 \end{bmatrix} ,$$

where

$$J = \frac{2}{1 + x^2 + y^2} .$$

If $\hat{\alpha}$ denotes the inclination of the streamline with

$$\frac{dY}{dX} = \tan \hat{\alpha} ,$$

then the irrotationality condition becomes

$$\frac{\partial q_c}{\partial n} = q_c \left[\frac{\partial \hat{\alpha}}{\partial s} - \frac{1}{J} \frac{\partial J}{\partial n} \right] .$$

We have already noted that when

$$\frac{\partial q_c}{\partial n} < 0$$

at the body, shock-free cross flow on a general cone is impossible, and hence, for cones with

$$\frac{1}{R} - \frac{\partial J}{\partial n} < 0 \tag{2.12}$$

shock free cross flow is impossible.

We note that

$$\frac{\partial}{\partial s} = \frac{1}{J} \cos \hat{\alpha} \frac{\partial}{\partial X} + \frac{1}{J} \sin \hat{\alpha} \frac{\partial}{\partial Y} \quad ,$$

$$\frac{\partial}{\partial n} = -\frac{1}{J} \sin \hat{\alpha} \frac{\partial}{\partial X} + \frac{1}{J} \cos \hat{\alpha} \frac{\partial}{\partial Y} \quad ,$$

$$ds^2 = J^2 (dX^2 + dY^2) \quad ,$$

and R is the radius of curvature of the image of the cone in the stereographically projected plane. Thus, cones that satisfy the above rule will not have a shock-free cross-flow.

We will now show that this condition is not satisfied on a circular cone. Consider a circular cone of half angle ψ_c . Then the radius of the circle on the stereographically projected plane is

$$a = \tan \frac{\psi_c}{2}$$

since

$$\psi_c < 90^\circ \quad , \quad a < 1 \quad .$$

Thus, on the body

$$J = \frac{2}{1+a^2}$$

and

$$\frac{\partial q_c}{\partial n} = \frac{q_c}{J} \left(\frac{1}{a} - Ja \right) > 0 \quad .$$

CHAPTER 3

THE NUMERICAL METHOD

In this chapter, a numerical method for the calculation of cones of arbitrary section at angle of attack is described. All the shock waves are captured correctly by making the scheme to be fully conservative¹³. In isentropic computations one chooses to conserve mass instead of momentum across the shock waves so that the shock position will be correctly represented. The resulting normal-momentum jump will then represent the "isentropic wave drag".

The method used here is distinguished from finite-difference methods by two unique features. The grids for the surface portion is generated separately, so that the main code is entirely independent of the shape of the cone; the differential equation is satisfied in the integral form and, thus, solid boundary conditions are implemented in a straightforward way.

3.1 The Finite Area Method

The conventional finite-volume method¹⁴ (for 2-D) could be extended to a vector field defined on a non-Euclidian space as long as we have a similar partial differential equation. In this section a finite area method on a unit sphere is developed. It should be emphasized, however, that the derivation would be the same for a vector field on a general curved surface. Let us assume that a smooth grid is generated over the computational portion of the sphere and

that the surface coordinates θ^α (latitude θ , longitude ψ) are provided at the nodal points:

$$\theta^\alpha = \begin{pmatrix} \theta \\ \psi \end{pmatrix}$$

In order to implement the finite area method, the coordinate cells are mapped to a square using a local bilinear transformation in the parametric space (see Figure 4). Since the partial differential equation is second order, the integration is performed over a secondary interlocking flux cell, as shown in Figure 5. The potential is defined on the nodes of coordinate cell and the flow and the geometric quantities are defined at the center of these cells in the mapped space. The local bilinear transformation is represented by

$$\theta = \sum_{i=1}^4 s^i \theta^i \quad \text{and} \quad \psi = \sum_{i=1}^4 s^i \psi^i .$$

Here, i denotes the nodal values and

$$s^i = 4 \left(\frac{1}{4} + \xi^i \xi \right) \left(\frac{1}{4} + \eta^i \eta \right) .$$

The geometric quantities can be calculated in the following manner. The metric tensor in the spherical coordinate system, θ^α is

$$\bar{g}_{\alpha\beta} = \begin{bmatrix} \sin^2 \psi & 0 \\ 0 & 1 \end{bmatrix} \quad (3.1)$$

and

$$\sqrt{\bar{g}} = \sin \psi . \quad (3.2)$$

In a mapped coordinate system, Ξ^α , the metric tensor is

$$g_{\alpha\beta} = \bar{g}_{\lambda\mu} \frac{\partial\theta^\lambda}{\partial\xi^\alpha} \frac{\partial\theta^\mu}{\partial\xi^\beta} \quad (3.3)$$

and

$$\sqrt{g} = \sqrt{\bar{g}} J \quad .$$

Here, J is the Jacobian of the parametric transformation $\theta^\alpha(\xi^\beta)$, i.e.,

$$\sqrt{g} = \sin\psi (\theta_\xi \psi_\eta - \theta_\eta \psi_\xi) \quad . \quad (3.4)$$

Because the geometric quantities are always evaluated at the center of the cells, the bilinear transformation and its best linear substitute have the same role¹⁵. Thus we take

$$s^i = s_b = \frac{1}{4} + \xi^i \xi^i + \eta^i \eta^i$$

and thus,

$$\theta_\xi^i = \sum_{i=1}^4 \theta^i \xi^i, \quad \text{etc.}, \quad (3.5)$$

and at the center of the cell

$$\theta = \frac{1}{4} \sum_{i=1}^4 \theta^i, \quad \text{etc.} \quad (3.6)$$

Equations (3.1) - (3.6) define the geometric quantities at the center of primary cells. The flow quantities may be calculated as follows: Let f be the disturbance to the freestream potential f_∞ due to the body, i.e., $F = f_\infty + f$. Then we assume the disturbed potential also to have the bilinear form

$$f = \sum_{i=1}^4 s^i f^i \quad .$$

Thus at the center of the cells,

$$f_\xi^i = \sum_{i=1}^4 \xi^i f^i, \quad \text{etc.},$$

and

$$f_{\xi\eta} = 4 \sum_{i=1}^4 \xi^i \eta^i f^i .$$

Here, again, if $f_{\xi\eta}$ is not needed in the formulation, then best linear variation of f is implied.

The total velocity is calculated from

$$V^\alpha = g^{\alpha\beta} \left[\frac{\partial f_\infty}{\partial \Xi^\beta} + \frac{\partial f}{\partial \Xi^\beta} \right]$$

and

$$f_\infty = \cos\alpha_A \cos\psi + \sin\alpha_A \sin\theta \sin\psi$$

where α_A is the angle of attack.

We are now ready to implement the finite area method. We integrate the weak conservation law over a domain Ω bounded by a curve c on the surface, so that

$$\int_{\Omega} \left(\frac{1}{\sqrt{g}} \frac{\partial \rho \sqrt{g} V^\alpha}{\partial \Xi^\alpha} + 2\rho F \right) d\Omega = 0 ;$$

applying surface divergence theorem to the first term, we find

$$\int_c \rho V^\alpha n_\alpha ds + \int_{\Omega} 2\rho F d\Omega = 0 .$$

This relation is valid for any arbitrary Ω and, therefore, also valid locally for a flux cell. Since flux-cell faces are parallel to coordinate lines in the mapped plane, we obtain, using one-point evaluation for each integral,

$$\delta[\rho\sqrt{g}U] + \delta[\rho\sqrt{g}V] + (2\rho\sqrt{g}F)_0 = 0 \quad (3.7)$$

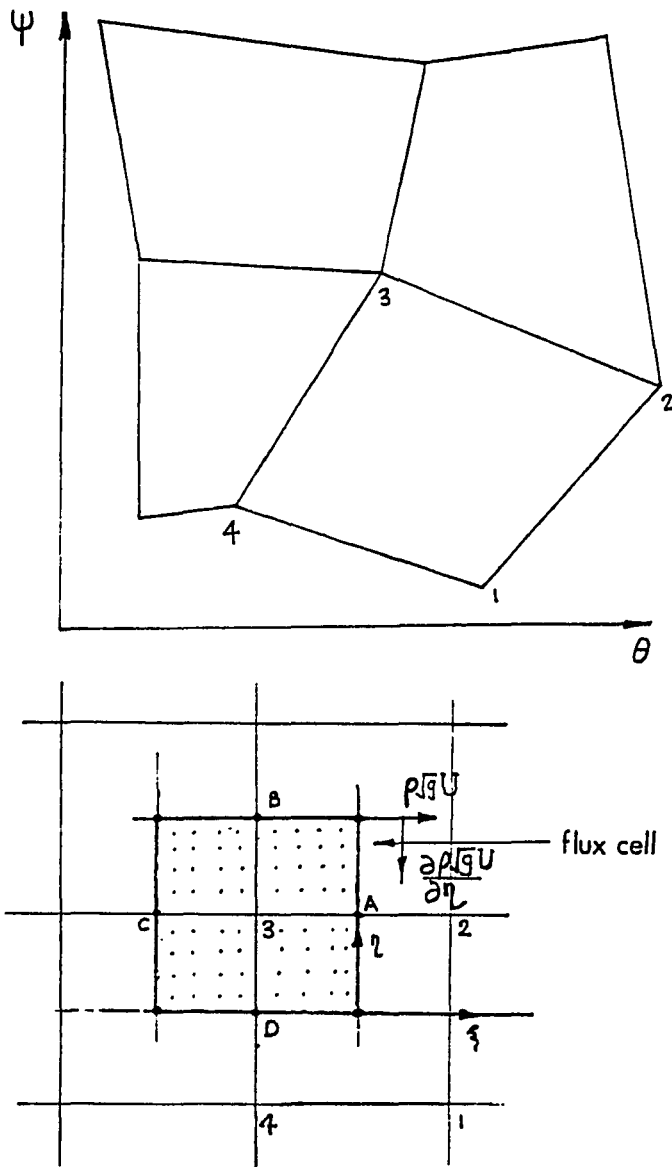


Figure 5. Sketch of primary cells and the flux cell.

for each cell where $\delta[\dots]$ denotes the net flux changes across the cell and $(\dots)_0$ the average over the cell. We also need to define the flux quantities at points A, B, C and D of the flux-cell faces. Since the flow quantities are defined at the center of primary cells, the simplest approximation to the Equation (2.1) is then

$$\mu_{\eta} \delta_{\xi} (\rho \sqrt{g} U) + \mu_{\xi} \delta_{\eta} (\rho \sqrt{g} V) + \mu_{\xi} \mu_{\eta} (2\rho \sqrt{g} F) = 0 \quad (3.8)$$

where μ and δ are respectively the averaging and central-difference operators.

We note here that the term $F_{\xi\eta}$ is not used in this simplified formulation. One could introduce this coupling by adding a lumping term derived by shifting the flux terms (as shown in Figure 5):

$$-\frac{1}{2} \varepsilon_L \delta_{\xi\eta} [(A_{\xi} + A_{\eta}) \delta_{\xi\eta} F - B_{\xi} \delta_{\eta} \mu_{\xi} F - B_{\eta} \delta_{\xi} \mu_{\eta} F] \quad (3.9)$$

where

$$A_{\xi} = \rho \sqrt{g} \left(g^{11} - \frac{U^2}{a^2} \right)$$

$$A_{\eta} = \rho \sqrt{g} \left(g^{22} - \frac{V^2}{a^2} \right)$$

$$B_{\xi} = \rho \sqrt{g} \frac{UF}{a^2}$$

$$B_{\eta} = \rho \sqrt{g} \frac{VF}{a^2}$$

and ε_L is an adjustable parameter such that $0 \leq \varepsilon_L \leq 1/2$. An alternative and perhaps much better, albeit expensive, method is to use higher-order integration. Another feature of Equation (3.7) is that it does not satisfy the freestream condition identically, and this could be

corrected by subtracting the freestream error

$$\mu_{\eta} \delta_{\xi}(\sqrt{g}U_{\infty}) + \mu_{\xi} \delta_{\eta}(\sqrt{g}V_{\infty}) + \mu_{\xi} \mu_{\eta}(2\sqrt{g}f_{\infty}) \quad (3.10)$$

from Equation (3.7).

3.2 Boundary Conditions

We consider the computational domain shown in Figure 4. The outer boundary C_0 is taken well outside the bow shock wave. Boundaries C_1 and C_2 are symmetry planes and C_b is the cone body where the normal velocity vanishes.

3.2.1 Outer Boundary. At the outer boundary, all the disturbance vanishes, i.e., f , f_{ξ} , f_{η} are all zero. This is implemented by setting the reduced potential to zero on two outer grid rings, i.e., if N_2 grids are the rings, then

$$f(I, N_2 + 1) = f(I, N_2 + 2) = 0$$

3.2.2 Symmetry Plane. At the symmetry plane, we introduce an additional grid line and explicitly set the reduced potential to be the same on two lines. Thus, if N_1 grids are in the circumferential direction, then

$$f(1, J) = f(3, J) \quad \text{and} \quad f(N_1 - 1, J) = f(N_1 + 1, J)$$

3.2.3 Cone Surface. On the body surface the normal velocity should be zero. If $B(\xi^{\alpha})$ is the cone surface, then $U^i \frac{\partial B}{\partial x^i} = 0$ implies $V^{\alpha} \frac{\partial B}{\partial \xi^{\alpha}} = 0$ since the body is a cone. If the body coincides with a coordinate surface, ξ for example, then $B(\xi^{\alpha}) = \eta = 0$ and the boundary condition implies $V = 0$, i.e., the contravariant cross-flow component that does not lie on the body must vanish. This is

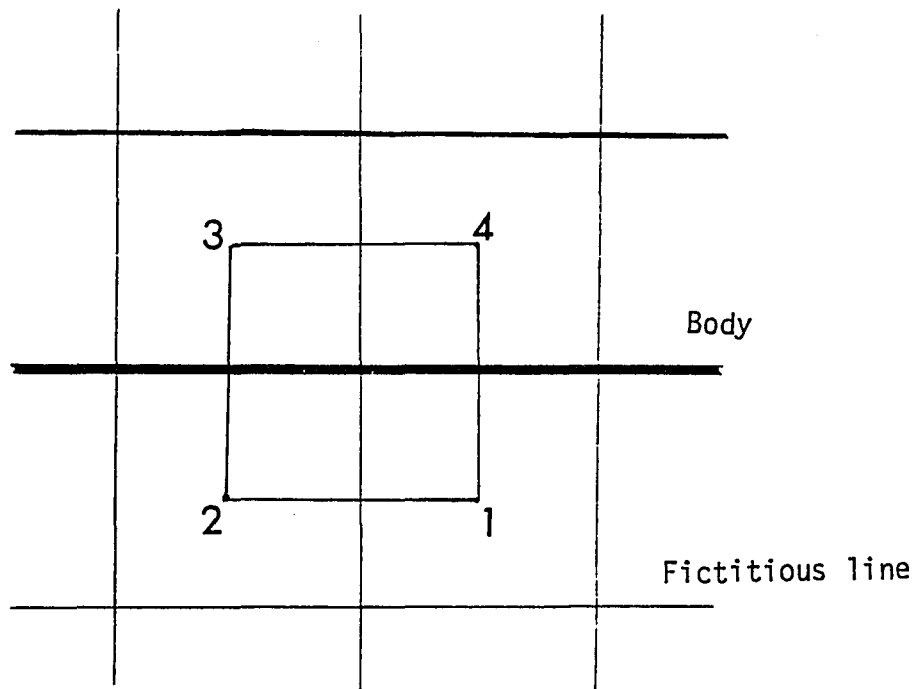


Figure 6. Flux cell arrangements at the body.

implemented by using flux reflections in the following way. Let us assume that a fictitious line is introduced below the boundary, as shown in Figure 6. The relevant condition is then

$$(\rho\sqrt{g}U)_1 = (\rho\sqrt{g}U)_4 \quad ,$$

$$(\rho\sqrt{g}U)_2 = (\rho\sqrt{g}U)_3 \quad ,$$

$$(\rho\sqrt{g}V)_1 = - (\rho\sqrt{g}V)_4 \quad ,$$

$$(\rho\sqrt{g}V)_2 = - (\rho\sqrt{g}V)_3 \quad ,$$

$$(2\rho\sqrt{g}F)_1 = (2\rho\sqrt{g}F)_4 \quad ,$$

and

$$(2\rho\sqrt{g}F)_2 = (2\rho\sqrt{g}F)_3 \quad .$$

This method enables one to implement the boundary condition without introducing any special coding routines.

3.3 Artificial Viscosity and Upwind Differencing

The governing partial differential equation becomes hyperbolic in the cross-flow supersonic zones and the finite area method is only conditionally stable in these zones. Also, at the sonic lines, the characteristics form a cusp normal to the cross-flow streamlines, and thus it is impossible to achieve stability without some kind of backward differencing in the time-like direction. In general, the crossflow streamline (the time-like direction) does not coincide with a coordinate direction, and thus the best way to perform the backward differencing is to upwind difference the f_{SS} term (rotated differencing)¹⁶. The scheme also needs to have a few other essential features. At the shock waves, the gradients are high and

the resultant high-frequency errors need to be stabilized. In addition, one needs to implement the entropy condition¹⁷ somehow to eliminate unphysical expansions. All the above requirements can be met by a simple modification of the scheme that also preserves the conservative nature of the method.

We noticed earlier that the higher-order terms of the governing partial differential equations are analogous to plane transonic flows. Thus, if we desymmetrize the above scheme by upwinding f_{SS} with first-order accuracy, then the resultant truncation errors will look like the viscous terms for plane transonic flows and, therefore, may be expected to capture any shock waves and insure the entropy condition.

These considerations motivated Grossman¹⁸ to develop a quasi-linear finite-difference method for this problem. However, both the difference main scheme and the artificial viscosity should be in the conservation form so that no source-like terms are introduced at the shocks, and this can be done in the following way. We explicitly add to the residual a viscosity term that is first-order (at least near the shocks) and that could effectively represent f_{SS} with an upwind bias. When we are working in a transformed space where the mesh size is unity, the following elegant structure exists for the above modification procedure. Consider the case of $V^\alpha > 0$. We noticed earlier that the terms contributing the f_{SS} term have a structure containing $-(\tilde{P} + \tilde{Q})$ and, therefore, will effectively be evaluated as $-\tilde{P}_{ij} - \tilde{Q}_{ij}$ in the finite-area scheme. To upwind with first-order accuracy, we

need to replace them by $-\tilde{P}_{i-1,j} - \tilde{Q}_{i,j-1}$, and this means we need to add a conservative viscosity T_{ij} , such that $T_{ij} = (\tilde{P}_{ij} - \tilde{P}_{i-1,j}) + (\tilde{Q}_{ij} - \tilde{Q}_{i,j-1})$, to the residual R_{ij} . Here the terms \tilde{P}_{ij} and \tilde{Q}_{ij} are evaluated in the following manner:

$$\tilde{P}_{ij} = \mu_{ij} \left[\frac{\rho\sqrt{g}U^2}{a^2} \delta_{\xi\xi} f + \frac{\rho\sqrt{g}UV}{a^2} \delta_{\xi\eta} f \right] ,$$

$$\tilde{Q}_{ij} = \mu_{ij} \left[\frac{\rho\sqrt{g}UV}{a^2} \delta_{\xi\eta} f + \frac{\rho\sqrt{g}V^2}{a^2} \delta_{\eta\eta} f \right] .$$

We define the switching function as

$$\mu_{ij} = \begin{cases} 1 - \frac{1}{M_c^2} \cdots \cdots & \text{for } (i,j) \text{ supersonic point.} \\ 0 \cdots \cdots & \text{for } (i,j) \text{ subsonic point.} \end{cases}$$

and the coefficients appearing in \tilde{P}_{ij} and \tilde{Q}_{ij} are calculated at a nodal point as the average of their values at the neighboring cell centers.

The method has to be appropriately modified for other directions of contravariant velocities. For later reference let us note that, in the limit, the above procedure induces an artificial viscosity of the form:

$$\mu \frac{\rho\sqrt{g}}{a^2} [|U| (UF_{\xi\xi\xi} + VF_{\xi\xi\eta}) + |V| (UF_{\xi\eta\eta} + VF_{\eta\eta\eta})] \times (\text{Mesh Size})$$

The above method makes the scheme first-order everywhere in the cross-flow supersonic zones. However, one could devise a hybrid scheme that is almost second-order by adding a second-order viscosity in the smooth hyperbolic regions and gradually switching to first

order near the shocks. We consider again the case $V^\alpha > 0$ and mesh size unity.

We notice, as before, that the terms \tilde{P}_{ij} and \tilde{Q}_{ij} (and therefore, f_{SS}) could be represented with second-order accuracy by the upwind terms in the form $2\tilde{P}_{i-1,j} - \tilde{P}_{i-2,j}$ and $2\tilde{Q}_{i,j-1} - \tilde{Q}_{i,j-2}$ respectively. Thus, we need to add a conservative second-order quantity in the form

$$\tilde{P}_{ij} - 2\tilde{P}_{i-1,j} + \tilde{P}_{i-2,j} + \tilde{Q}_{ij} - 2\tilde{Q}_{i,j-1} + \tilde{Q}_{i,j-2} .$$

In order to change from this to first-order viscosity near the shocks, we use this in the hybrid form

$$\begin{aligned} HT_{ij} = & [\{\tilde{P}_{ij} - (1-A)\tilde{P}_{i-1,j}\} - \{\tilde{P}_{i-1,j} \\ & - (1-A)\tilde{P}_{i-2,j}\}] + [\{\tilde{Q}_{ij} - (1-B)\tilde{Q}_{i,j-1}\} \\ & - \{\tilde{Q}_{i,j-1} - (1-B)\tilde{Q}_{i,j-2}\}] , \end{aligned}$$

where $A = \lambda_1 \rho_\xi$ and $B = \lambda_2 \rho_\eta$ are the shock detection functions. λ_1, λ_2 are $O(1)$ parameters and should be chosen such that $A \approx 1$, $B \approx 1$ near the shocks. Thus, in the smooth regions, $A \approx 0$, $B \approx 0$ and scheme will be second-order, and near the shocks it will be first-order.

3.4 Construction and Analysis of the Iterative Scheme

The scheme devised in the previous chapters will give us a nonlinear system of algebraic equations to solve. We note here that the boundaries separating the elliptic and hyperbolic zones, the location of shock waves and the time-like direction of hyperbolic points are not known a priori, and in general, cross-flow streamlines

do not coincide with any of the grid lines. Because of this complexity, we need to solve this system of equations by an iterative procedure even in the hyperbolic zones.

Thus, the iteration procedure has to be very carefully constructed to avoid instability, especially in the cross-flow supersonic zones. On the other hand, we need a scheme that is reasonable fast. The method chosen here is a line relaxation procedure with three grid levels. Once this method has been validated and the numerical behavior of the code is well understood, one could use a multigrid procedure to accelerate the solution procedure.

The line relaxation procedure constructed here is different and much more involved than the conventional methods. First, we note that an iterative procedure for a steady problem could be considered equivalent to a problem of evolution in an artificial time. A suitable unsteady problem for our case may be found in an indirect way. We assume that the flow field is being solved by discretizing the partial differential equation in its quasilinear form using Jameson's rotated-difference scheme along with his special relaxation method. The corresponding artificial evolution problem will then give us a suitable time dependent partial differential equation. The stability properties of the unsteady equation presented by Jameson was with respect to Cartesian velocities of the specific problem and, thus, does not give much insight into the algorithm. In this section, the construction and analysis is presented in detail in terms of general variables. Let us consider the Cauchy problem for the partial differential equation describing the local evolution of the error $E(\bar{x}^\alpha, t)$

$$\begin{aligned}
AE_t + BE_{\xi t} + CE_{\eta t} &= \left[g^{\alpha\beta} - \frac{V^\alpha V^\beta}{a^2} \right] \frac{\partial^2 E}{\partial \xi^\alpha \partial \xi^\beta} \\
&+ \epsilon \mu \left[\frac{U^2}{a^2} E_{\xi\xi\xi} + \frac{UV}{a^2} (E_{\xi\xi\eta} + E_{\xi\eta\eta}) + \frac{V^2}{a^2} E_{\eta\eta\eta} \right]
\end{aligned}$$

with

$$E(\xi^\alpha, 0) = \phi(\xi^\alpha)$$

where μ is the switching function and $\epsilon(>0)$, is a small parameter representing the mesh size. We will assume $V^\alpha > 0$. Terms in the left-hand side will depend on the type of iterative procedure, and the second term in the right-hand side is due to the artificial viscosity obtained by upwind differencing. We will analyze the local behavior of this equation by freezing the coefficients.

Fourier transformation gives

$$\hat{E}(k, t) = \hat{\phi}(k) e^{(\sigma+i\omega)t}$$

where σ can be easily shown to be

$$\begin{aligned}
\sigma &= \frac{-A \left[\left(g^{11} - \frac{U^2}{a^2} \right) k_1^2 + 2 \left(g^{12} - \frac{UV}{a^2} \right) k_1 k_2 + \left(g^{22} - \frac{V^2}{a^2} \right) k_2^2 \right]}{A^2 + (Bk_1 + Ck_2)^2} \\
&- \frac{\epsilon \mu (Bk_1 + Ck_2) \left[\frac{U^2 k_1^3}{a^2} + \frac{UV}{a^2} (k_1^2 k_2 + k_1 k_2^2) + \frac{V^2 k_2^3}{a^2} \right]}{A^2 + (Bk_1 + Ck_2)^2}
\end{aligned}$$

Therefore the L_2 norm provides

$$\|\hat{E}(k, t)\|_2 = \|\hat{\phi}(k) e^{\sigma t}\|_2$$

and if $\sigma \leq 0$ and $t > 0$, then

$$\|E(\Xi^\alpha, t)\|_2 \leq \|E(\Xi^\alpha, 0)\|_2$$

Thus, the partial differential equation is well posed in the sense of L_2 if the condition on $\sigma < 0$ is satisfied. Now we note that at subsonic cross-flow points, the polynomial $\left(g^{11} - \frac{U^2}{a^2}\right)k_1^2 + 2\left(g^{12} - \frac{UV}{a^2}\right)k_1k_2 + \left(g^{22} - \frac{V^2}{a^2}\right)k_2^2$ is positive definite and, therefore, if we choose the term $A \geq 0$, we will satisfy the above inequality. However, of supersonic cross-flow points this polynomial is indefinite and we thus choose the relations

$$A = 0, \quad B \geq 0 \quad \text{and} \quad C \geq 0.$$

We note here that in smooth supersonic cross-flow regions, the above choice of parameters will give an almost undamped equation. Near the shock waves, frequencies are high due to large gradients and from the expression for σ we note that these modes are heavily damped since $\sigma \sim -k^2$ for large k . We will now further analyze the partial differential equation in the smooth regions with the viscous terms ignored. Transforming the equation to the streamwise coordinate system,

$$AE_t + 2B_1E_{st} + 2B_2E_{nt} = (1 - M_c^2)E_{ss} + E_{nn}.$$

It is easy to find the other principal coordinate that reduces this equation to the canonical form

$$(M_c^2 - 1)E_{ss} - E_{nn} - \left(\frac{B_1^2}{M_c^2 - 1} - B_2^2\right)E_{TT} + AE_T = 0$$

where

$$T = t + \frac{B_1}{(1-M_c^2)} s + B_2 n \quad .$$

At subsonic cross-flow points T is the time-like direction. However, at supersonic cross-flow points, either s or n could be made the time-like direction by appropriately choosing B_1 and B_2 . We choose s to be the time-like direction so that the unsteady problem will be compatible with the steady problem. This means we need the condition

$$B_1^2 > (M_c^2 - 1) B_2^2$$

at the supersonic cross-flow points.

When constructing the iteration scheme, one should make sure that the resultant unsteady equation will satisfy the above conditions in order to obtain convergence to the steady solution.

The equation of the characteristic cone could be easily derived from the canonical form of the partial differential equation and is given by

$$(M_c^2 - 1)(t^2 + 2B_2 nt) - 2B_1 st + (B_2 s - B_1 n)^2 = 0 \quad .$$

This cone touches the plane $t = 0$ along the line $n = \frac{B_2}{B_1} s$. The most retarded characteristic can be found by maximizing t/s with respect to n/s and is given by

$$n = -\frac{B_2}{B_1} s \quad \text{and} \quad t = \frac{2B_1}{(M_c^2 - 1)} s \quad .$$

Implications of these results on the convergence mechanism will be clearly seen once the difference scheme is constructed.

When the partial differential equation is discretized in its quasilinear form, central differences are used everywhere except at the supersonic points where the term contributing to the f_{ss} term are upwind-differenced. From this difference equation one should construct the line relaxation procedure such that the resultant unsteady equation will satisfy all the conditions derived before.

We will now construct the iteration scheme to sweep circumferentially from windward to leeward in lines. We consider the case of $V^\alpha > 0$. At subsonic cross-flow points we will use,

$$f_{\xi\xi} = f_{i-1,j}^+ - 2\tilde{f}_{ij} + f_{i+1,j} \quad ,$$

$$f_{\eta\eta} = f_{i,j+1}^+ - 2f_{ij}^+ + f_{i,j-1} \quad ,$$

and

$$f_{\xi\eta} = \frac{1}{4} [f_{i+1,j+1}^+ - f_{i-1,j+1}^+ - f_{i+1,j-1}^+ + f_{i-1,j-1}^+] ,$$

where f^+ denotes the new level and f the update such that

$$f_{ij}^+ = f_{ij} + \omega_R (\tilde{f}_{ij} - f_{ij}) \quad :$$

Here, ω_R is the over-relaxation factor and is > 1 . When updating the scheme at supersonic cross-flow points, we make sure that the number of old and new values cancel in each term so that the effective contributions to the term E_t would be zero. Thus, we take for the f_{ss} contribution

$$f_{\xi\xi} = 2f_{ij}^+ - f_{ij} - 2f_{i-1,j}^+ + f_{i-2,j} \quad ,$$

$$f_{\eta\eta} = 2f_{ij}^+ - f_{ij} - 2f_{i,j-1}^+ + f_{i,j-2} \quad ,$$

$$f_{\xi\eta} = 2f_{ij}^+ - f_{ij} - f_{i-1,j}^+ - f_{i,j-1}^+ + f_{i-1,j-1} \quad ,$$

and for f_{nn} contributions,

$$f_{\xi\xi} = f_{i-1,j}^+ - f_{ij}^+ - f_{ij} + f_{i+1,j} \quad ,$$

$$f_{\xi n} = \frac{1}{4} [f_{i+1,j+1} - f_{i-1,j+1}^+ - f_{i+1,j-1} + f_{i-1,j-1}^+] ,$$

$$f_{nn} = f_{i,j+1}^+ - 2f_{i,j}^+ + f_{i,j-1}^+ \quad .$$

We may now write the iterative scheme for finite-area method

as

$$\begin{aligned} & A_1 C_{ij} + A_2 (C_{ij} - C_{i-1,j}) + A_3 (C_{ij} - C_{i,j-1}) \\ & + A_4 (C_{ij} - C_{i,j+1}) = R_{ij} + T_{ij} + A_5 (C_{i-1,j-1} \\ & - C_{i-1,j+1}) \quad , \end{aligned}$$

where,

$$C_{ij} = f_{ij}^+ - f_{ij}$$

is the correction.

If we consider that $R_{ij} + T_{ij}$ are equivalent to their quasi-linear finite difference equivalents multiplied by $\rho\sqrt{g}$, then the updating procedure described above will give the following values for

$A_1 \dots A_5$:

$$A_1 = \begin{cases} \rho\sqrt{g} \left(g^{11} - \frac{V^2}{a^2} \right) \left(\frac{2}{\omega_R} - 1 \right) & \text{subsonic cross-flow} \\ 0 & \text{supersonic cross-flow} \end{cases}$$

$$A_2 = \rho\sqrt{g} \left(g^{11} - \frac{U^2}{a^2} + 3\mu \frac{U^2}{a^2} + 2\mu \frac{UV}{a^2} \right) \quad ,$$

$$A_3 = \rho\sqrt{g} \left(g^{22} - \frac{V^2}{a^2} + 3\mu \frac{V^2}{a^2} + 2\mu \frac{UV}{a^2} \right) ,$$

$$A_4 = \rho\sqrt{g} \left(g^{22} - \frac{V^2}{a^2} + \mu \frac{V^2}{a^2} \right) ,$$

$$A_5 = \frac{1}{2} \rho\sqrt{g} \left(g^{12} - \frac{UV}{a^2} + \mu \frac{UV}{a^2} \right) .$$

This scheme should be modified when V changes sign.

We could get further insight into this scheme by looking at the equivalent time dependent equation. This is obtained by taking the limit $\Delta t, \Delta \xi, \Delta \eta \rightarrow 0$,

$$C_{ij} = \left(\frac{f_{ij}^+ - f_{ij}}{\Delta t} \right) \Delta t = \frac{\partial f}{\partial t} \Delta t, \quad \text{etc.}$$

Thus, the local error equation will be

$$\begin{aligned} \Delta t \left\{ \left(g^{11} - \frac{U^2}{a^2} \right) \left(\frac{2}{\omega_R} - 1 \right) E_t - \frac{V}{\sqrt{g}q_c} E_{nt} \right. \\ \left. + \frac{U}{q_c} (1 - M_c^2) E_{st} \right\} = (1 - M_c^2) E_{ss} + E_{nn} \end{aligned}$$

for subsonic points and

$$\begin{aligned} \Delta t \left\{ - \frac{V}{\sqrt{g}q_c} E_{nt} - \frac{2(U+V)}{q_c} (1 - M_c^2) E_{st} \right\} \\ = (1 - M_c^2) E_{ss} + E_{nn} \end{aligned}$$

for supersonic points.

Note that the quantity $\left(g^{11} - \frac{U^2}{a^2} \right)$ is positive definite at subsonic cross-flow points and, therefore, as long as $\omega_R < 2$, the coefficient of E_t will be positive. At supersonic cross-flow points

the gradients in the s direction are larger than those in the n direction. The above consideration gives us the following model equation for the error near the shocks in the supersonic zone:

$$2 \left(\frac{\Delta t}{\Delta s} \right) \left(\frac{U+|V|}{q_c} \right) E_{st} = - E_{ss} + \Delta s E_{sss}$$

Fourier transformation gives us

$$\hat{E}(k,t) = \hat{E}(k,0) \exp \left(\left[- \left(2 \frac{\Delta s^2}{\Delta t} \left\{ \frac{q_c}{U+|V|} \right\} k^2 \right) - i \left(2 \frac{\Delta s}{\Delta t} \left\{ \frac{q_c}{U+|V|} \right\} k \right) \right] t \right)$$

This tells us the kind of damping provided by the scheme near the shocks. Here the change of sign of the velocity V (contravariant component that does not lie in the sweep direction) does not affect the damping. But if the sign of U changes (sweeping against the flow), then the scheme could become unstable. This becomes an important factor in choosing the type of sweep for high angle of attack cases.

Next we will verify the compatibility condition derived before. In order to make s as the time-like direction in unsteady problems as well, we need the inequality

$$4 \left(\frac{U+V}{v} \right)^2 g (M_c^2 - 1) > 1$$

to be satisfied at supersonic points in the cross flow.

To ensure that the above condition is always satisfied, especially near the sonic line, we further augment the E_{st} term by adding $\lambda \frac{(U+V)}{q_c} f_{st}$ where λ is as small as possible and yet sufficient to ensure stability. The term f_{st} has to be represented by an upwind

difference, so we write this as

$$\lambda \left(\frac{U+V}{q_c} \right) \left[\frac{U}{q_c} (C_{ij} - C_{i-1,j}) + \frac{V}{q_c} (C_{ij} - C_{i,j-1}) \right] .$$

Finally, we will study the characteristic cone of the artificial time-dependent equations. From our earlier results we know that the characteristic cone touches the (s,n) plane along the line

$$t = 0 \quad \text{and} \quad n = \frac{-v}{2\sqrt{g} (U+|V|)(M_c^2-1)} s$$

at supersonic cross-flow points and

$$t = 0 \quad \text{and} \quad n = \frac{-v}{\sqrt{g} U (1-M_c^2)} s$$

at subsonic cross-flow points.

Also, the most retarded characteristic is

$$n = \frac{v}{2\sqrt{g} (U+|V|) (M_c^2-1)} s$$

and

$$t = \frac{2 (U+|V|)}{q_c} s$$

at supersonic cross-flow points, and

$$n = \frac{v}{\sqrt{g} U (1-M_c^2)} s$$

and

$$t = - \frac{U}{q_c} s$$

for subsonic cross-flow points.

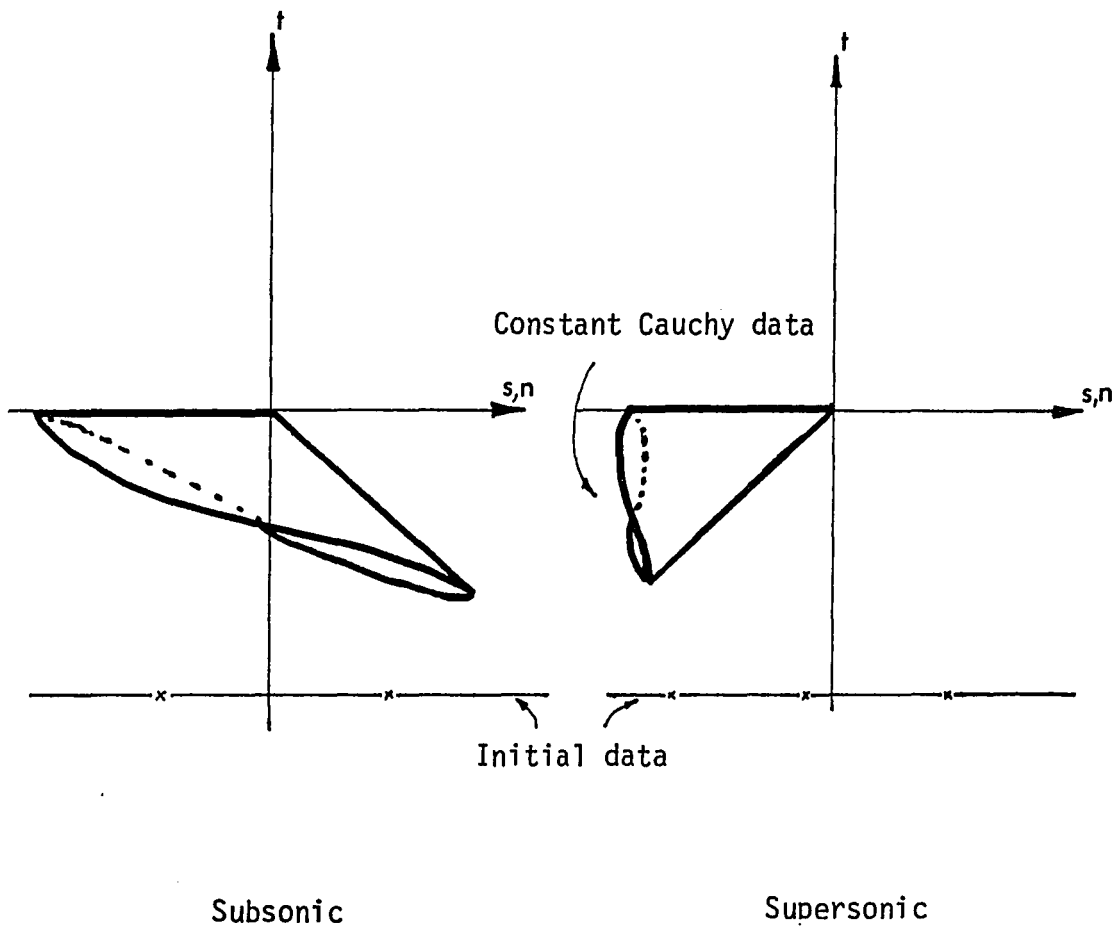


Figure 7. Unsteady characteristic cones for subsonic and supersonic points.

From the figure we can see that in smooth supersonic cross-flow regions, convergence occurs when the characteristic cone eventually ceases to touch the initial data plane and intersects the constant Cauchy data, as shown in Figure 7.

At subsonic cross-flow points, the characteristic cone angle will be greater than 90° and the convergence is due to damping introduced by the term f_t . We note here that the region of dependence in both supersonic and subsonic cross-flow points is a single line at the current level, and we need to update the points surrounding this line. Finally, we observe that the smaller the characteristic cone angle, the faster the convergence for cross-flow supersonic points. This means that adding additional f_{st} terms will slow down the scheme considerably, especially near $M_c \approx 1$.

3.5 Grid Generation

In this section, two efficient methods are described for the generation of grids over the computational portion of the unit sphere. Smooth grids improve the accuracy of finite area methods and almost orthogonal grids give good stability properties. It is desirable to have grids clustered wherever the flow properties vary rapidly (across shocks and near the body). In our case, however, the presence of the bow shock as well as the body shock makes it impossible to cluster the grids by simple means, because the location of these shocks is not known in advance. It was, therefore, decided to use almost uniform grids, and they have been found to give excellent results.

Suppose a special coordinate system ξ^α is chosen on the surface so that the metric tensor

$$g_{\alpha\beta} = \begin{bmatrix} J^2 & 0 \\ 0 & J^2 \end{bmatrix} ,$$

then ξ^α are called the isothermal coordinate system¹⁹, and this transformation maps the surface portion conformally to a plane. For a spherical surface, this could be done using a stereographic projection:

$$z = \xi + i\eta = \tan \frac{\psi}{2} e^{i\theta} .$$

Here z is a complex variable. At this stage we could take two different routes to generate the grids. The most straightforward way is to apply a conformal transformation followed by a simple shearing to obtain a rectangular region. A suitable conformal transformation is the "Joukowski transformation" and this would transform almost elliptical regions to almost circular shapes. Let

$$W(z) = Re^{i\phi} ,$$

then the Joukowski transformation could be written as

$$z = W + \frac{d^2}{W}$$

where $W = \sqrt{d^2}$ are singular points.

We could now transform the computational domain to a rectangular region by a simple shearing:

$$x = \phi$$

and

$$Y = \frac{R - R_{\text{body}}}{R_{\text{outer}} - R_{\text{body}}}$$

Here, R_{body} and R_{outer} can be obtained by spline fitting the body shape and the outer boundary. In the rectangular region obtained we generate uniform or nonuniform grids and thus obtain corresponding representations on the sphere.

This method is thus only suitable for straight wings of almost elliptic sections. For shapes that are highly cambered and complicated, a numerical grid generation method is needed. The method developed here can be considered an extension of Thompson's grid generation method²⁰ for curved surfaces.

Suppose we assume that the body-conforming coordinates x^α satisfy Laplace's equation in the isothermal coordinates ξ^α , i.e.,

$$\frac{\partial^2 x}{\partial \xi^\alpha \partial \xi^\beta} = 0$$

and

$$\frac{\partial^2 y}{\partial \xi^\alpha \partial \xi^\beta} = 0$$

in the computational domain. Then the solution of these equations will give us the coordinates of the grid points. Suppose we apply a transformation to interchange the dependent and independent variables.

We get

$$g^{\alpha\beta} \frac{\partial^2 \xi}{\partial x^\alpha \partial x^\beta} = 0$$

and

$$g^{\alpha\beta} \frac{\partial^2 \eta}{\partial x^\alpha \partial x^\beta} = 0 \quad ,$$

where

$$g_{\alpha\beta} = \frac{\partial \xi^\lambda}{\partial x^\alpha} \frac{\partial \xi^\lambda}{\partial x^\beta} \quad .$$

These two coupled, quasilinear, elliptic equations are to be solved in a rectangular domain with Dirichlet boundary conditions. In general, this procedure does not give orthogonal grids, but the maximum principle guarantees that the grids will not cross. Here we note that we began with an isothermal coordinate system to avoid grid distortion. The boundary conditions are provided, as before, by curve fitting the body and outer boundary. Simple clustering could easily be done with this method. Since the equations are elliptic they could be discretized using central differences and solved quite rapidly by a line-relaxation method.

CHAPTER 4

A DESIGN METHOD TO OBTAIN CONICAL WINGS WITH SHOCK-FREE CROSS-FLOW

As noted before, although conical wings with shock-free cross-flow are of practical interest, there is no evidence that such flows exist. However, one could devise a direct approach to search for such flows. Suppose we consider a test case with shocked cross-flow and change the gas law inside the cross-flow bubble in such a way that the resulting partial differential equation is elliptic; then the elliptic-to-elliptic transition will result in a smooth sonic surface. We may accept the solution outside this surface (which includes the bow shock wave and part of the cone) and use the flow properties on the surface to solve the Cauchy problem for the actual gas law (for the actual gas law the governing equation is hyperbolic) to obtain the new body shape inside the surface. However, one should note that in this method there is no guarantee that a certain gas law will provide Cauchy data that will provide a smooth flow up to the body. This method is still preferable because it is direct and only part of the configuration is being modified. This method has been successfully introduced to transonic flows by Sobieczky²². The application of this fictitious-gas method is not straightforward for conical flows for the following reasons. In plane transonic flow a sonic bubble is defined by the statement $Q \geq a^*$ where a^* is the speed of sound at the sonic condition and is a known constant. In conical flows, however, a^* varies and thus is an unknown.

This difficulty can be eliminated by first computing the actual speed of sound and, whenever it is less than the cross-flow velocity, replacing it by the fictitious speed of sound. When we change the gas law, we must take care to preserve mass conservation at the sonic line. In conical flows, because the density varies along the sonic line, the gas law should be chosen to give continuous density across the conic line. Let us first look at the simplest way to meet these requirements.

The energy equation is

$$M_{\infty}^2 a^2 = \rho^{\gamma-1} = 1 + \frac{\gamma-1}{2} M_{\infty}^2 (1 - q_c^2 - F^2) ,$$

and at sonic conditions

$$M_{\infty}^2 a_*^2 = \rho_*^{\gamma-1} = \frac{1 + \frac{\gamma-1}{2} M_{\infty}^2 (1 - F_*^2)}{\frac{\gamma+1}{2}} .$$

Thus, if we use the gas law of the form

$$M_{\infty}^2 a^2 = \rho^{\gamma-1} = \frac{1 + \frac{\gamma-1}{2} M_{\infty}^2 (1 - F^2)}{\frac{\gamma+1}{2}}$$

then the flow properties would be continuous across the sonic line and the resulting partial differential equation will have the form

$$g^{\alpha\beta} \frac{\partial^2 F}{\partial \xi^{\alpha} \partial \xi^{\beta}} + \dots = 0$$

and is elliptic. This could be called the incompressible analog for conical flows. In this scheme the artificial viscosity is switched off and the iteration coefficients are specialized to the case of $a \rightarrow \infty$. We will now examine a few other forms of the gas law. Let us consider the gas law

$$\rho^{\gamma-1} = M_{\infty}^2 q_c^2 .$$

Density is again continuous across the sonic line and the resulting partial differential equation is

$$\left(g^{\alpha\beta} + \frac{2V^{\alpha}V^{\beta}}{q_c^2 (\gamma-1)} \right) \frac{\partial^2 F}{\partial \Xi^{\alpha} \partial \Xi^{\beta}} + \dots = 0$$

and is of elliptic type. Of course, we switch off the viscosity and use the elliptic iteration coefficients with

$$a^2 = - \frac{q_c^2 (\gamma-1)}{2} .$$

One could use a gas law in a more general form as

$$M_{\infty}^2 a^2 = \rho^{\gamma-1} = \frac{[1 + \frac{\gamma-1}{2} M_{\infty}^2 (1 - F^2)]}{\frac{\gamma+1}{2}} - C (q_c^2 - a^2)$$

where the constant C should be chosen to give an elliptic equation. In changing the gas law inside the sonic surface, one needs to make sure that the gas law near the bow shock wave is correct. This was done by first solving the real problem to convergence, so that the bow shock and the cross-flow sonic bubble are well developed, and then using this as the initial condition to solve the problem with a fictitious gas law inside the sonic surface.

We will now consider the Cauchy problem for the cross-flow sonic bubble. In plane transonic flow, the best method for solving this problem is to apply the hodograph transformation to the partial differential equation and solve the resulting linear partial differential equations using the method of characteristics. Here the

simplicity is due to the homogeneous nature of the equations and also because only one stream function is necessary to describe the problem. This makes streamline tracing particularly easy. However, in conical flows the method of characteristics does not have any advantage because, as mentioned before, a Legendre transformation will not result in a linear equation and we also need two stream functions to describe the flow. It was, therefore, decided to solve this problem using a finite-difference marching method in a mapped zone, as shown in Figure 8. The easiest way to solve this problem is to use an explicit predictor-corrector method. However, if better stability properties are desired, one could use an implicit method. Writing the governing equation in the quasilinear form in full,

$$\left(g^{\alpha\beta} - \frac{V^\alpha V^\beta}{a^2} \right) \frac{\partial^2 F}{\partial \Xi^\alpha \partial \Xi^\beta} + (2 - M_c^2) F + \frac{1}{\sqrt{g}} V^\alpha \frac{\partial \sqrt{g}}{\partial \Xi^\alpha} + V_\alpha \frac{\partial g^{\alpha\beta}}{\partial \Xi^\beta} - \frac{V^\alpha V_\lambda V_\mu}{2a^2} \frac{\partial g^{\lambda\mu}}{\partial \Xi^\alpha} = 0 .$$

This, along with the irrotationality condition, could be written in the vector form as,

$$\frac{\partial V_\alpha}{\partial \eta} = A_{\alpha\beta} \frac{\partial V_\beta}{\partial \xi} + B_\alpha . \quad (4.1)$$

We will now develop a second-order-accurate method for the solution of Equation (4.1). Suppose V_α^0 , V_α^* and V_α^+ are the old, the predictor and the corrector level values, then

$$V_\alpha^* = V_\alpha^0 + \Delta\eta \left(\frac{\partial V_\alpha}{\partial \eta} \right)^0 \quad (4.2)$$

and

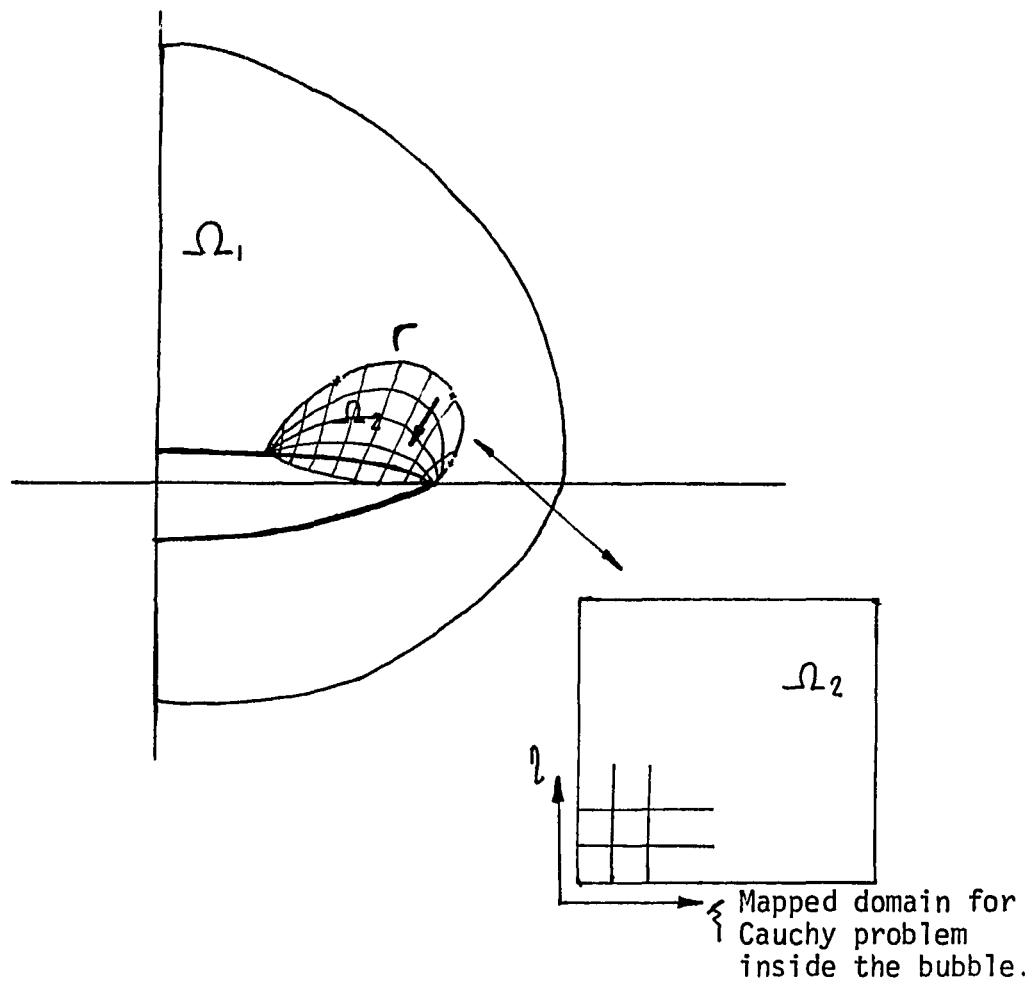


Figure 8. Regions Ω_1 and Ω_2 are calculated respectively by the usual algorithm and the marching algorithm.

$$V_{\alpha}^{+} = \frac{1}{2} \left[V_{\alpha}^0 + V_{\alpha}^{*} + \Delta\eta \left(\frac{\partial V_{\alpha}}{\partial \eta} \right)^{*} \right] . \quad (4.3)$$

Equations (4.2), (4.2) and (4.3) give us an explicit system to solve. At the old level, the derivative in the space-like direction is backward-differenced:

$$\left(\frac{\partial V_{\alpha}}{\partial \xi} \right)^0 = \left[(V_{\alpha})_{IJ} - (V_{\alpha})_{I-1,J} \right] \frac{1}{\Delta \xi} ;$$

and at the predictor level, forward-differenced:

$$\left(\frac{\partial V_{\alpha}}{\partial \xi} \right)^{*} = \left[(V_{\alpha})_{I+1,J} - (V_{\alpha})_{I,J} \right] \frac{1}{\Delta \xi} .$$

We use the same method to obtain the potential at the new level:

$$F^{*} = F^0 + \Delta\eta v^0$$

and

$$F^{+} = \frac{1}{2} [F^0 + F^{*} + \Delta\eta v^{*}] .$$

CHAPTER 5

RESULTS AND DISCUSSION

Computations were made to demonstrate that the method predicts qualitative features correctly and their quantitative aspects accurately. All calculations were performed on three mesh levels, starting with a 16 x 16 grid system. On this initial grid 150 iterations were performed and this was followed by 100 iterations at both the 32 x 32 and final level. Convergence for the last two grids is reliable after 30 to 50 iterations, depending on whether or not there is a body shock wave. The possible types of sweep are shown in Figure 9. It has been found through numerical experimentation that circumferential sweep gives the fastest convergence and is also more stable.

The first example is a circular cone of half angle 10° at Mach 2 and angle of attack 10° . Results are compared with Euler computation by D.J. Jones²², and it is seen that the agreement is excellent at all the grid levels. Since, in this case the cross flow is subsonic, convergence is quite rapid and on the 16 x 16 grid, 70 iterations were sufficient. This coarse grid requires only a few seconds in CDC 7600 CPU time. Cross-flow streamline patterns were obtained by integrating the velocity field, and Figure 12e compares these patterns for the 10° and 20° angle of attack cases. The lift-off phenomenon is clearly seen in the figure. The next series of

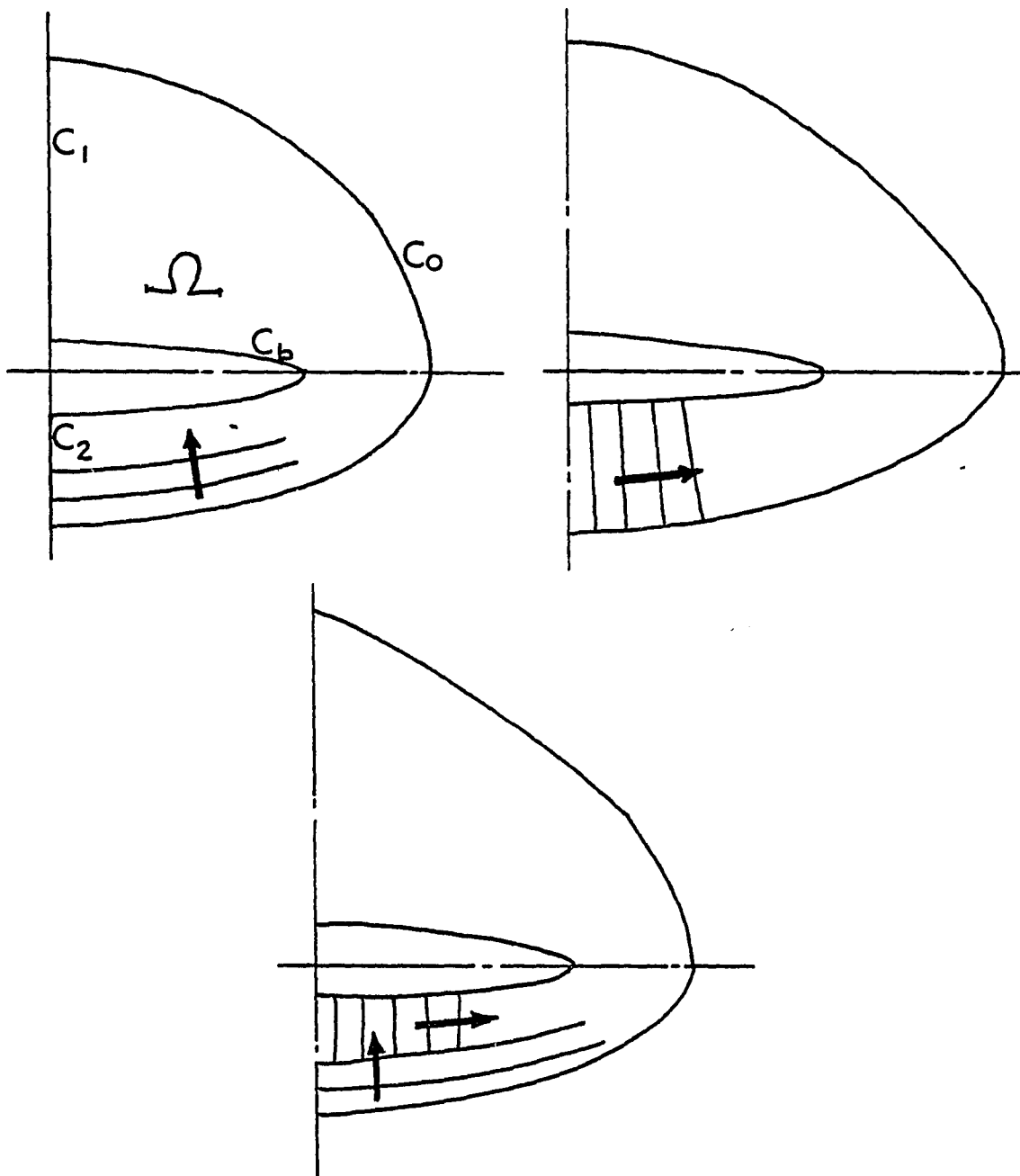


Figure 9. Computational boundaries and various possibilities for line relaxation.

figures show the result for a 6:1 elliptic cone at each mesh level. In this case, due to the body shock wave, resolution is good only at the final level. These results are compared with those obtained by Siclari using the Euler equations²³. The agreement is generally excellent except for the extra leading-edge suction, which may be a consequence of the potential approximation to the bow shock wave, and except for the post-shock pressure. We note here that the rotational calculation does not show the expected shock-foot singularity captured by the present irrotational calculations. The third example is a thin elliptic wing of major-to minor axis ratio 13:1. Figure 16d compares the Euler results of Siclari, the non-conservative potential finite-difference results of Grossman, and the present results. Here all three methods capture, to some extent, the shock-foot singularity. The finite area method agrees well with the rotational results. The difference in the shock position between the conservative and non-conservative method is to be noted. A few important observations are noted below.

It is often difficult to get the iteration scheme to converge for very thin wings with the coarse mesh due to the rapid expansion at the leading edge. One could introduce extra damping at the shock wave by an early switching to upstream differencing, but this could smear the shocks badly. The shock resolution of the present method is very good, with most shock waves only spanning two interior mesh points. Even with the fine mesh, the present method is an order of magnitude faster than the Euler-equation method on a coarser grid.

Results of the design procedure given here are limited. The simplest fictitious gas law has been used for circular cone at Mach 2 and 20° angle of attack. The shape of sonic surface on the cone using the real and fictitious gas laws are shown in Figures 17a and 17b, respectively. Figures 17c and 17d show the pressure distribution on the cone and on the modification of this cone that makes the flow shock-free. As in the planar case, only slight changes in body shape are required to eliminate the cross-flow shock wave.

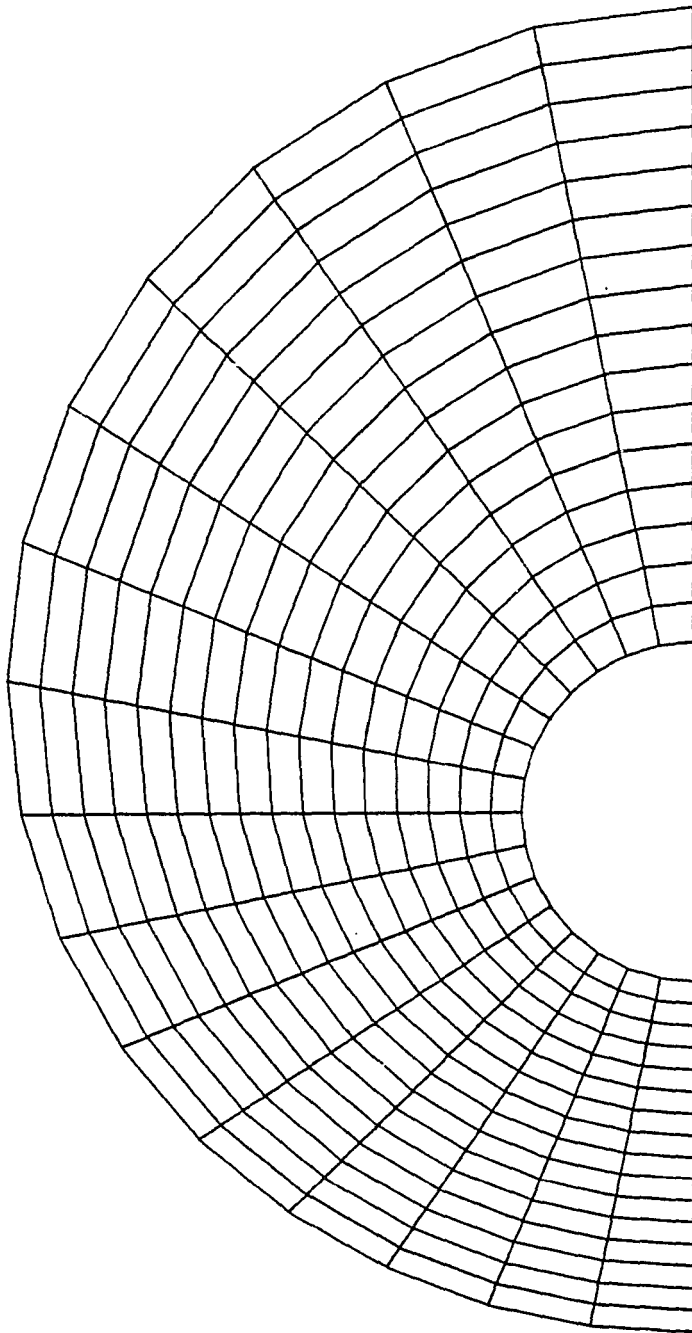


Figure 10a. The 16 x 16 mesh for a circular cone of 10° half angle, at 10° angle of attack.

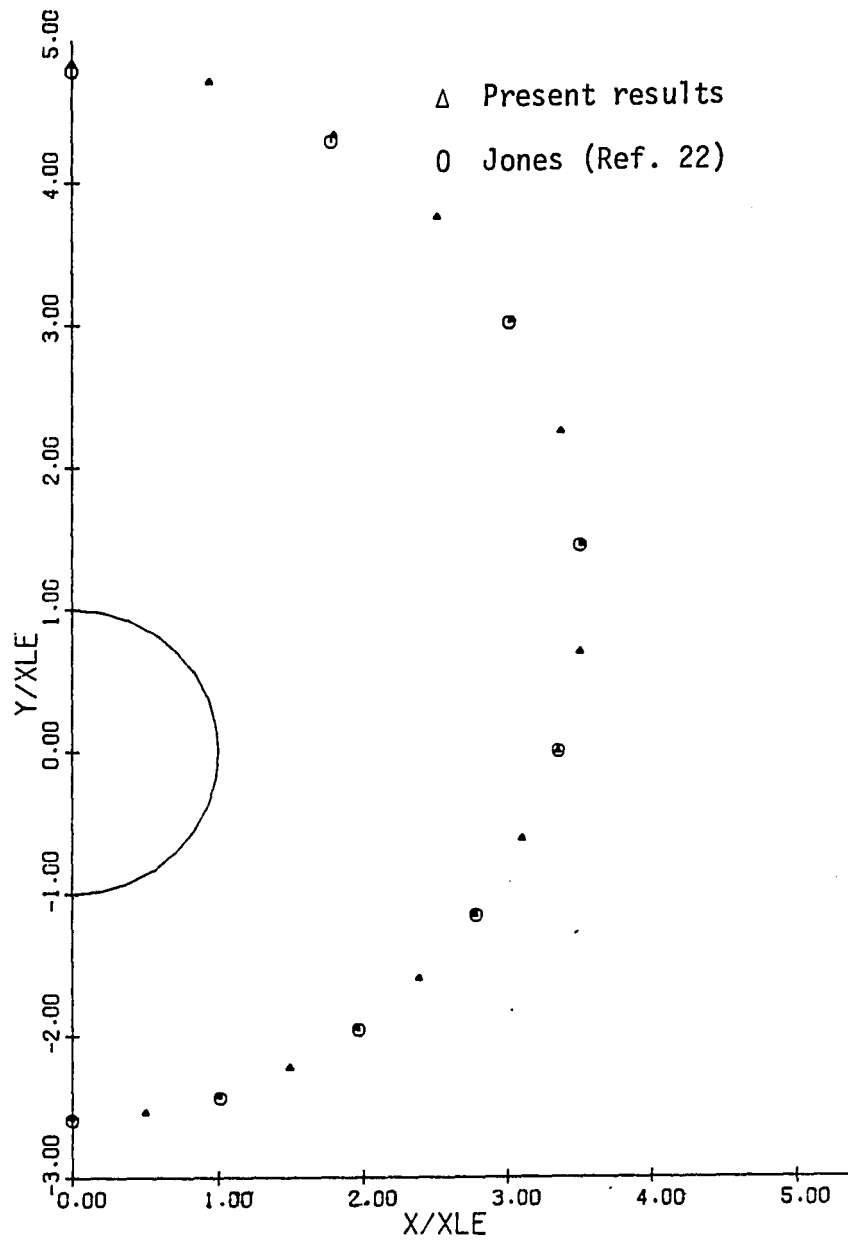


Figure 10b. Bow shock position for a circular cone at 10° angle of attack with $M_\infty = 2.0$. Comparison is with the rotational calculation of Jones²².

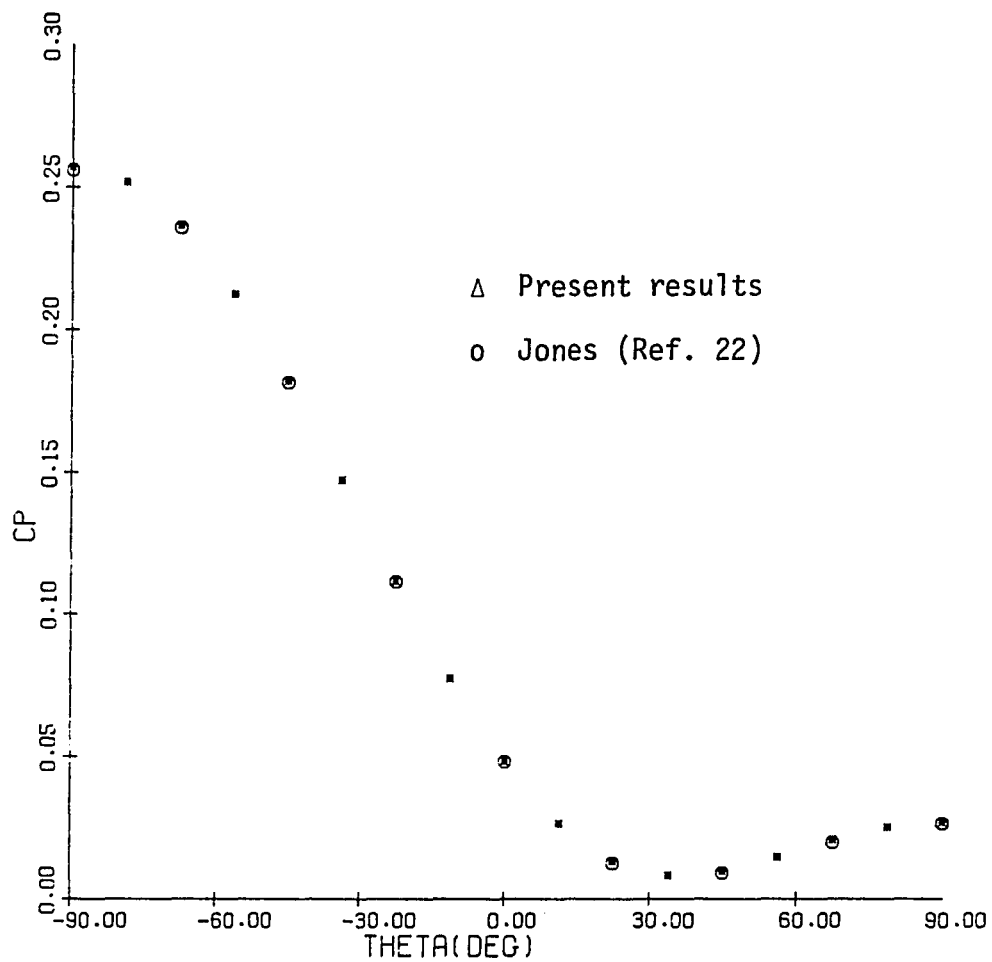


Figure 10c. Surface pressure distribution for a circular cone at 10° angle of attack with $M_\infty = 2.0$. Comparison is with the rotational calculations of Jones²².

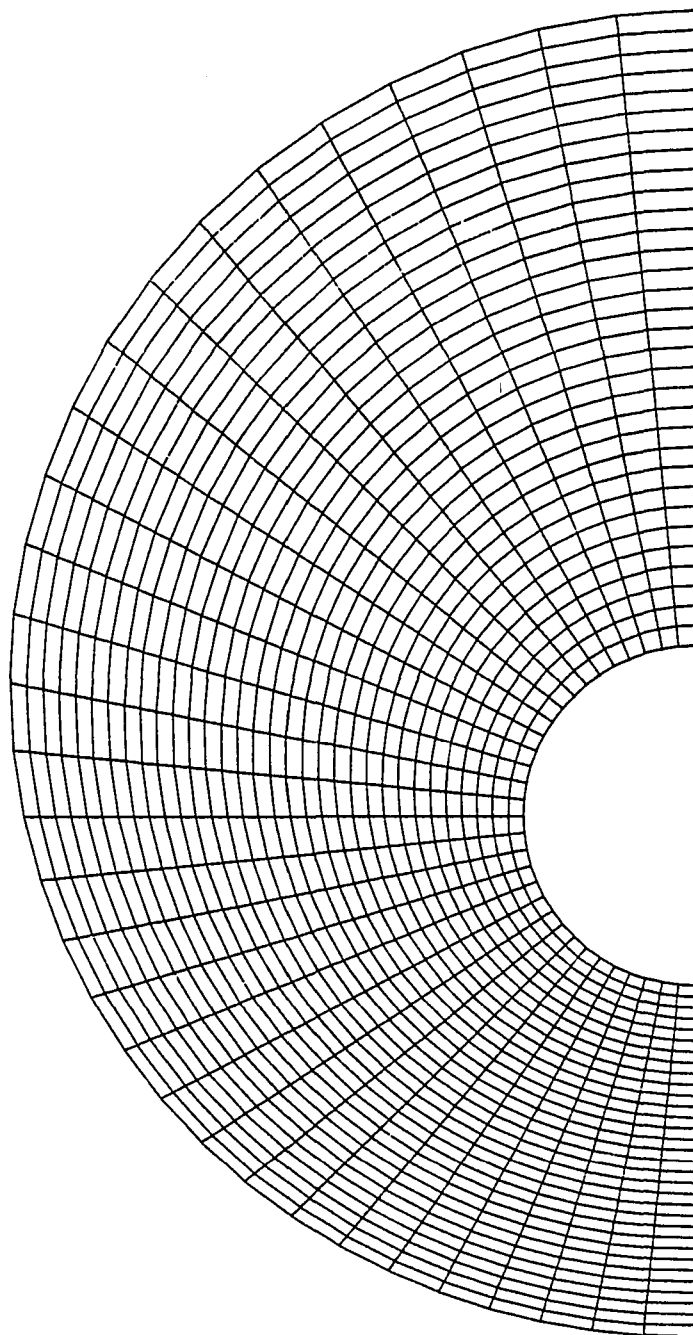


Figure 11a. The 32 x 32 mesh for a circular cone of 10° half angle, at 10° angle of attack.

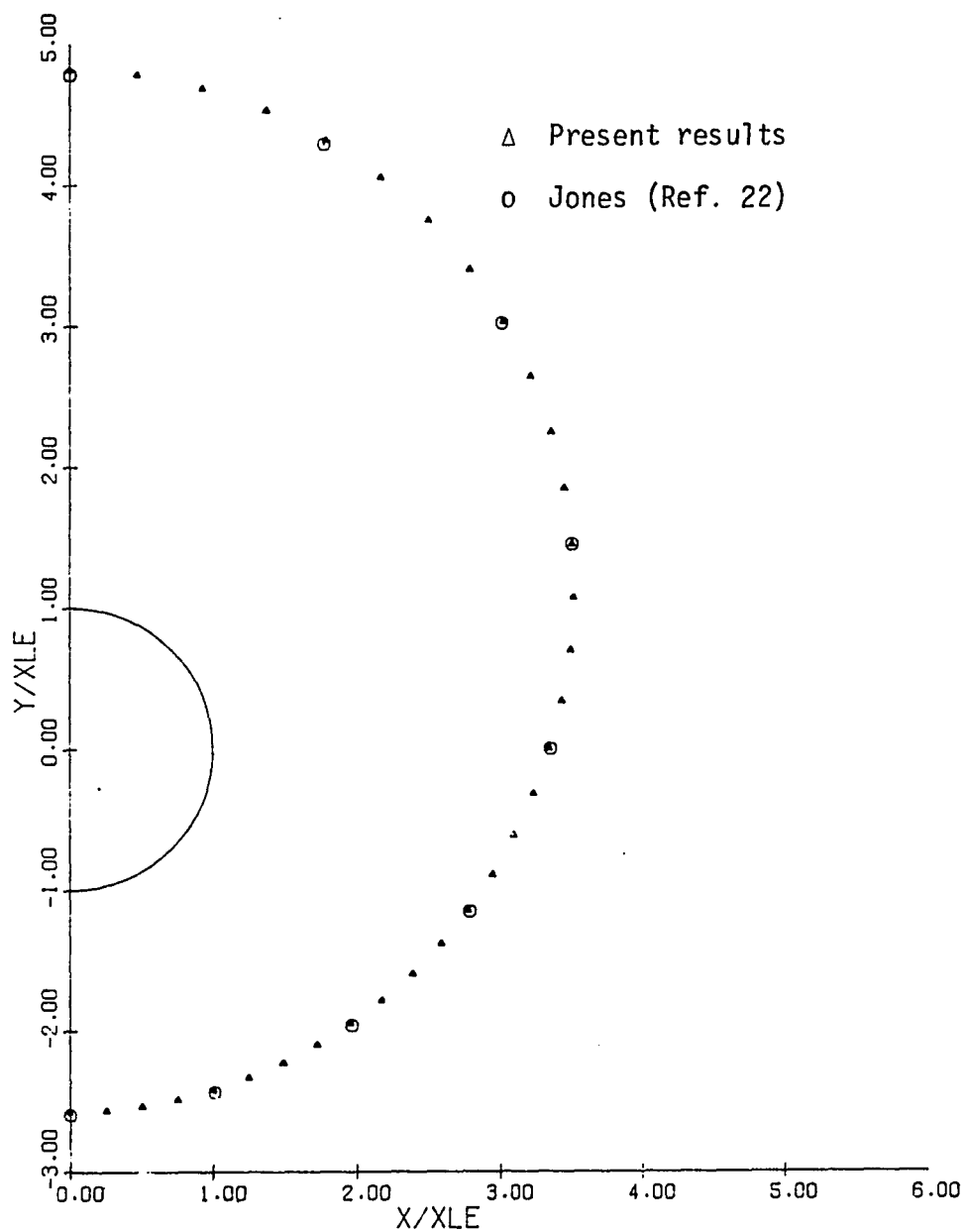


Figure 11b. Bow shock position for a circular cone at 10° angle of attack calculated using 32×32 mesh. Comparison is with the rotational calculations of Jones²².

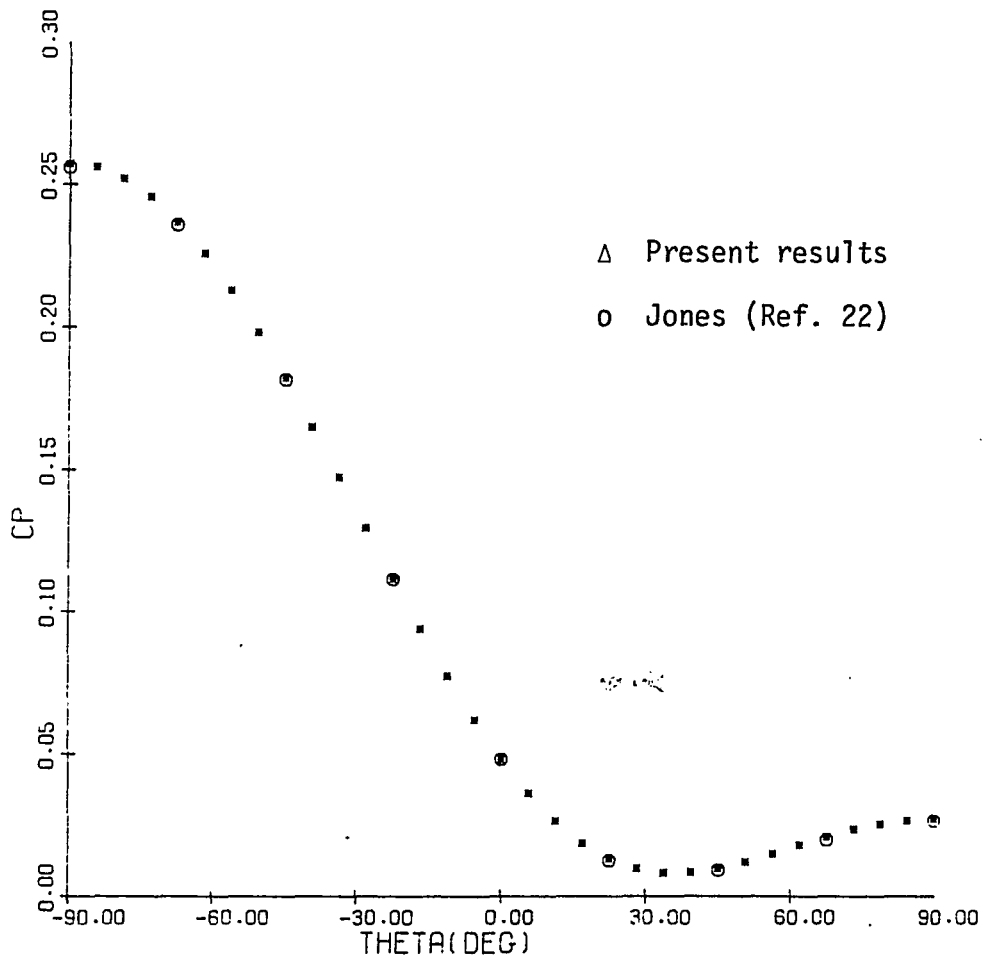


Figure 11c. Surface pressure distribution of a circular cone at 10° angle of attack at Mach 2, calculated using the 32×32 mesh. Comparison is with the rotational calculations of Jones²².

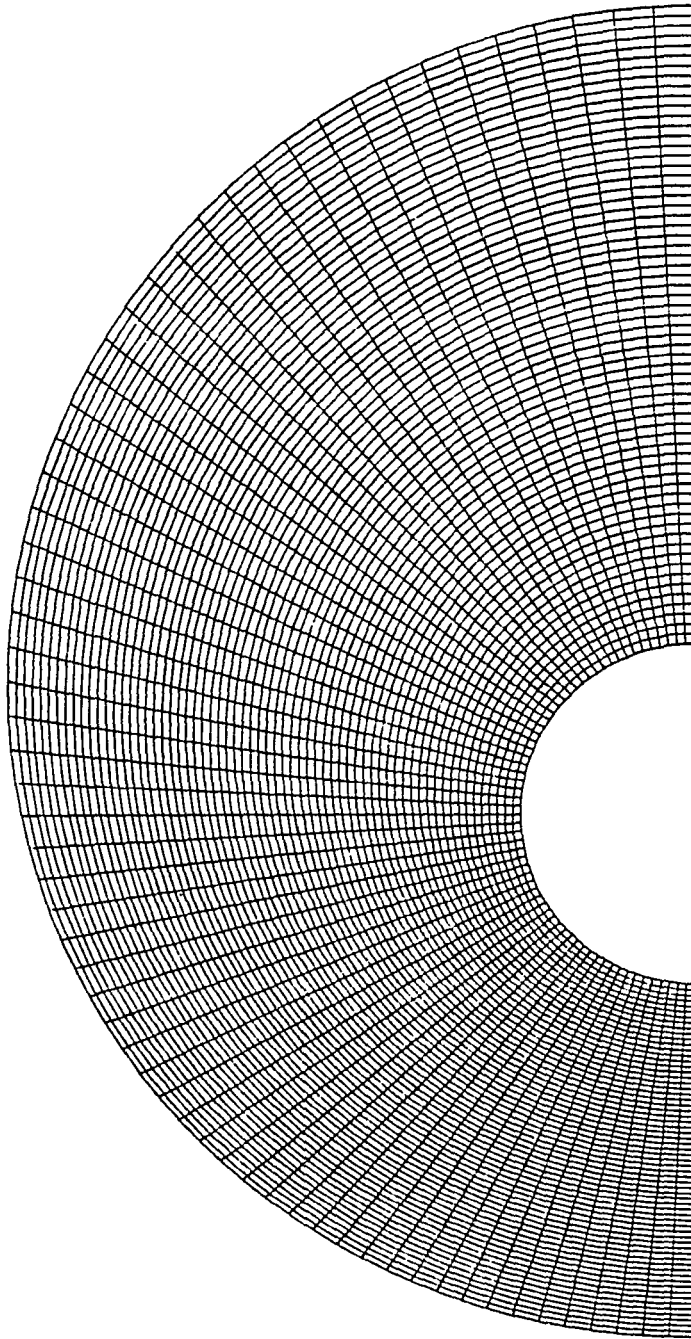


Figure 12a. The 64 x 64 mesh for a circular cone of 10° half angle, at 10° angle of attack.

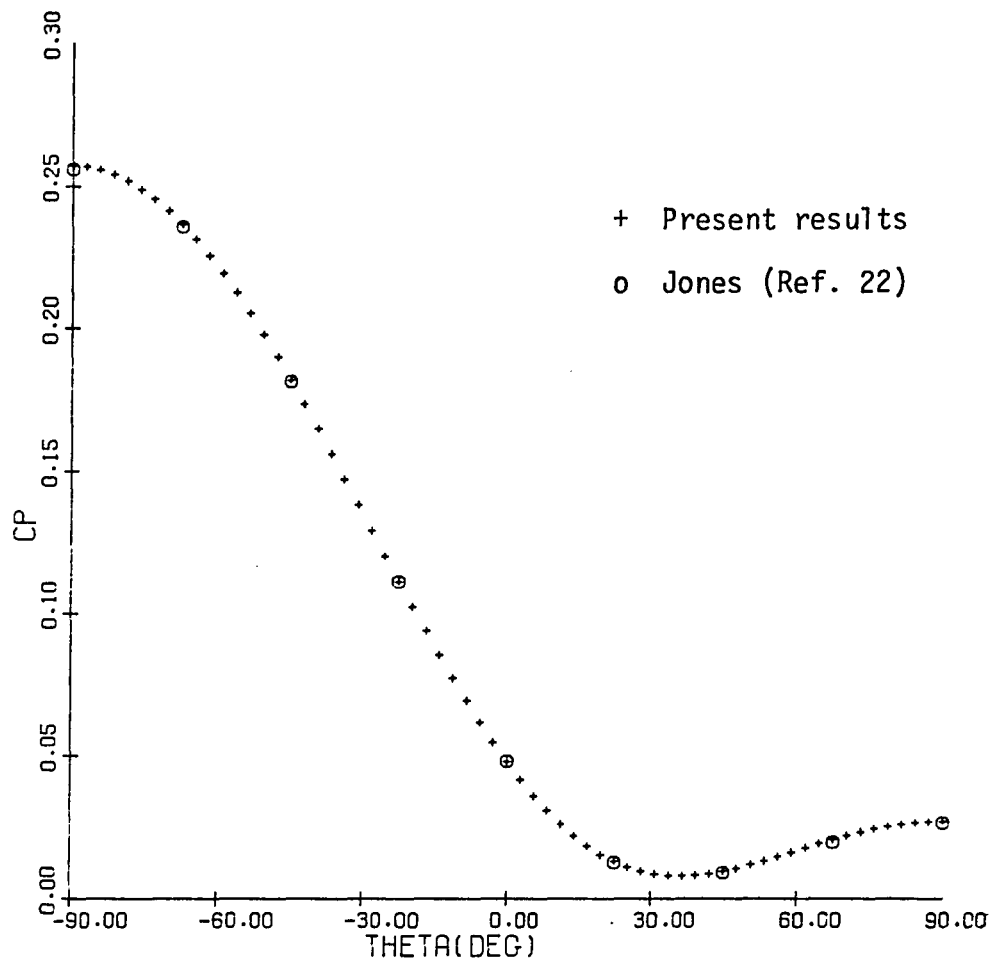


Figure 12b. Surface distribution for a circular cone at 10° angle of attack with $M_\infty = 2.0$; 64×64 grid. Comparison is with the rotational calculations of Jones²².

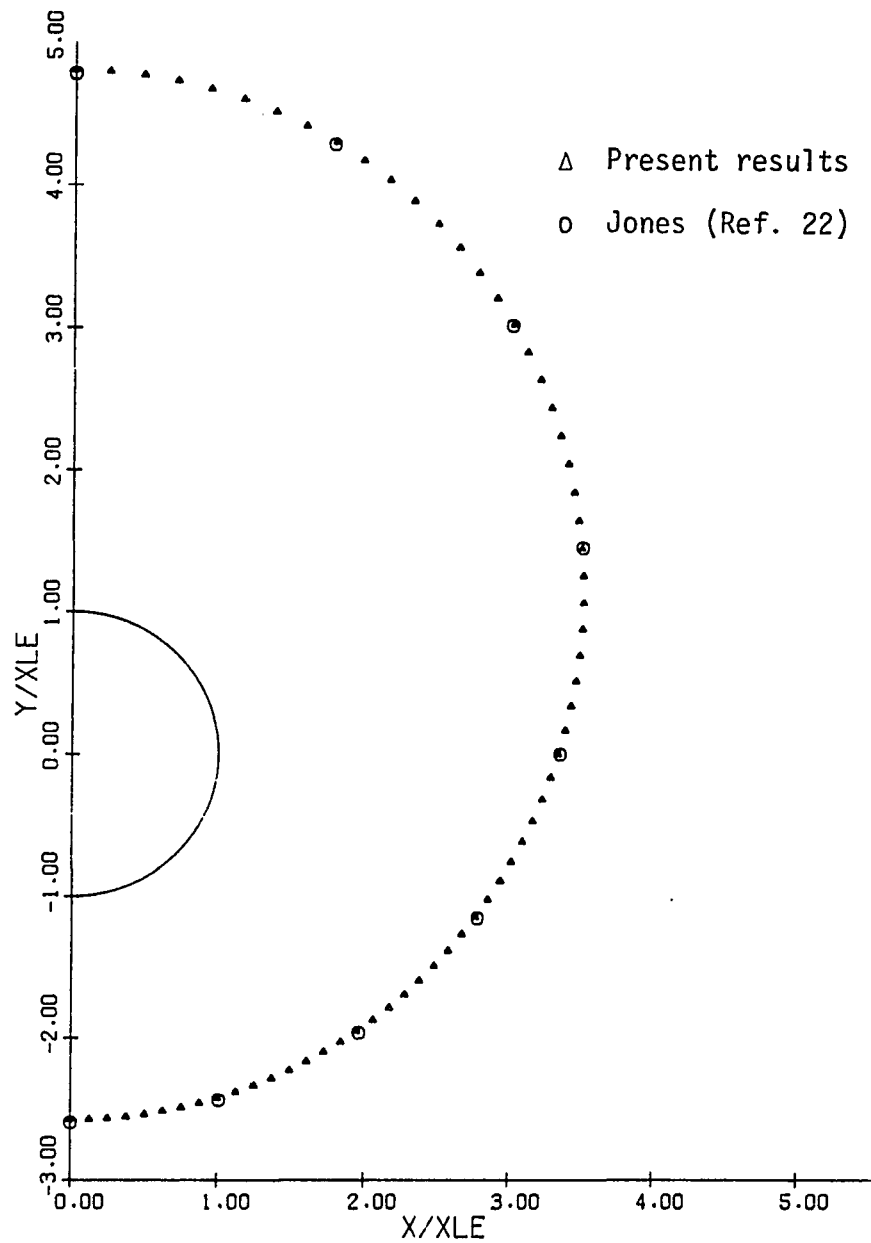


Figure 12c. Bow shock position for a circular cone of 10° half angle at 10° angle of attack. Calculated using a 64×64 grid. Comparison is with the rotational calculations of Jones²².

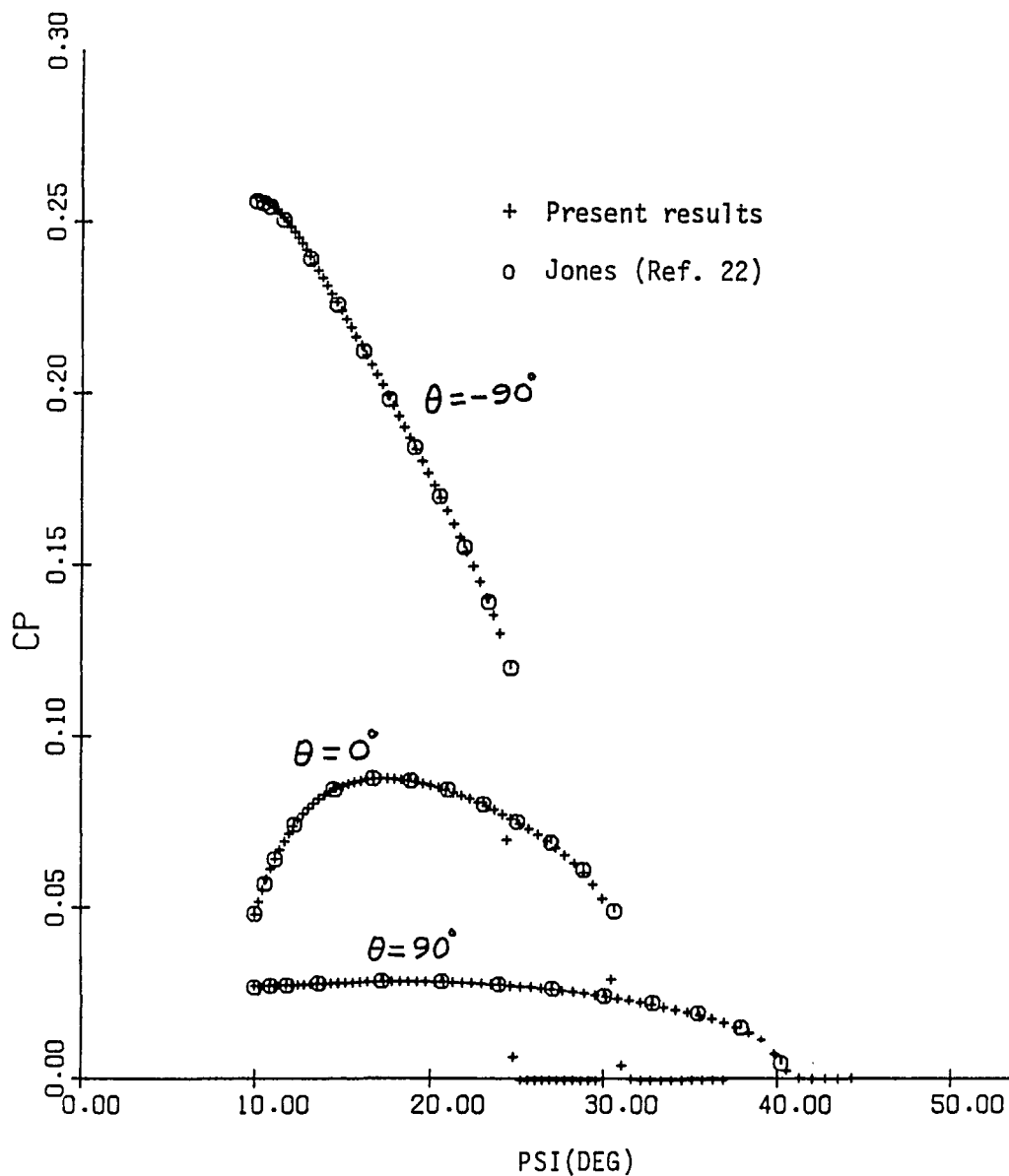


Figure 12d. Pressure variation between the bow shock wave and the body for a circular cone of 10° half angle at 10° angle of attack with $M_\infty = 2.0$. Comparison is with the rotational calculations of Jones²².

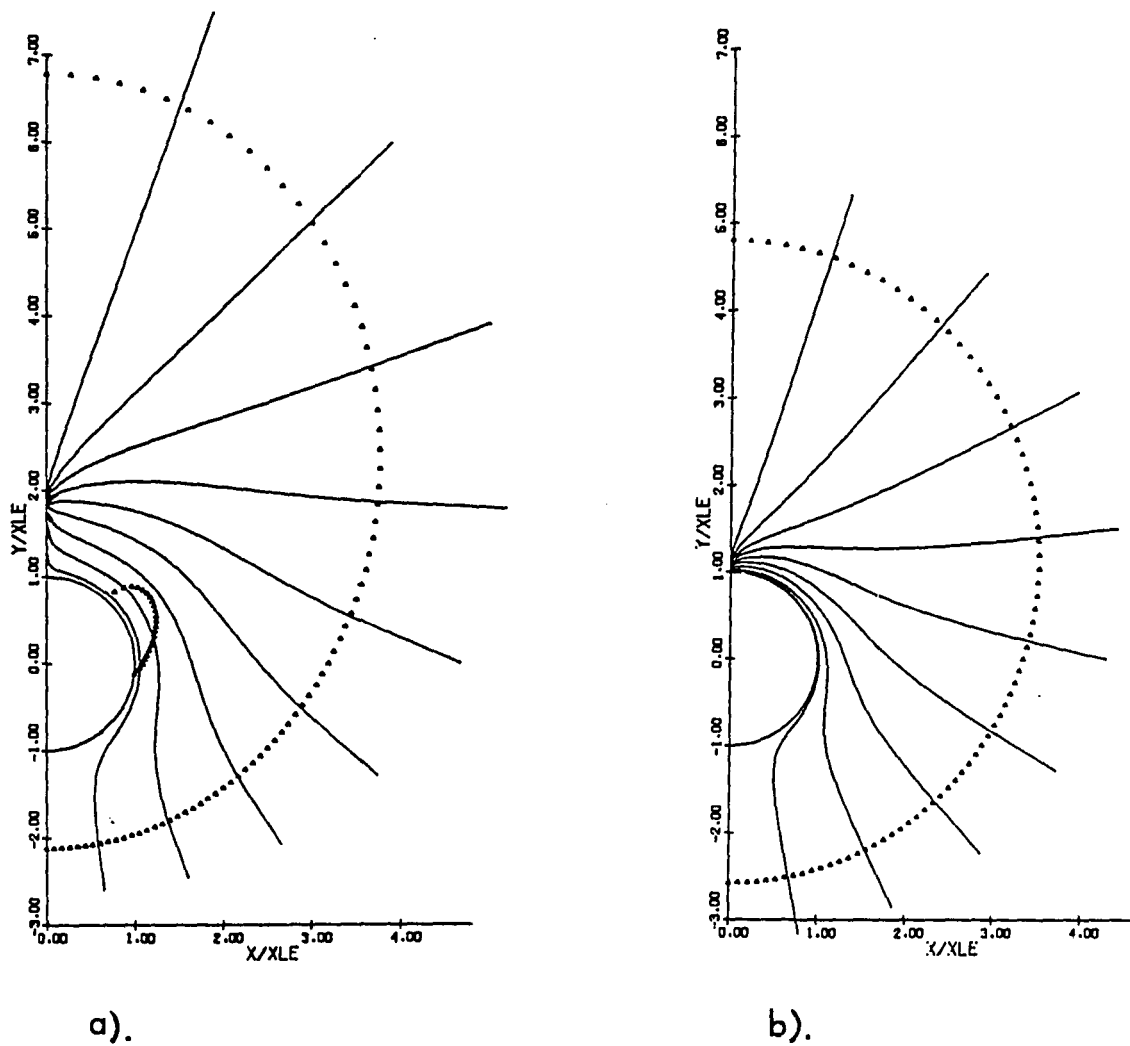


Figure 12e. Comparisons of the streamline patterns on a circular cone at a) 20° and b) 10° angle of attack with $M_\infty = 2.0$. Note the lift-off of the leeward note as well as the formation of a supersonic zone in the cross flow.

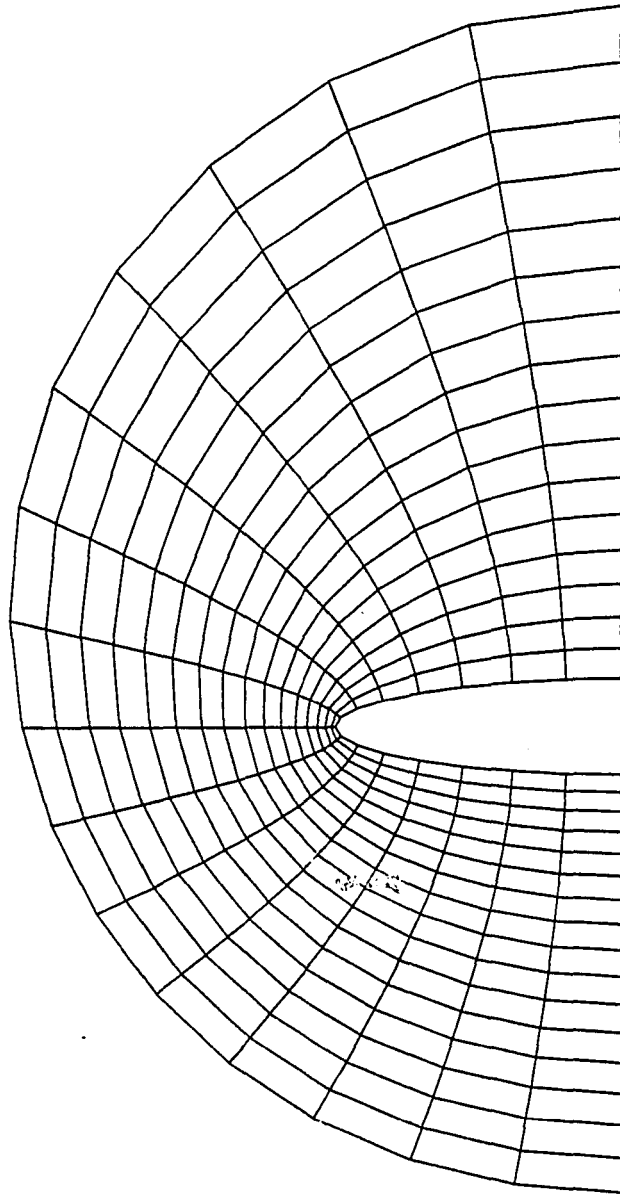


Figure 13a. The 16 x 16 mesh for a 6:1 elliptic cone at 10° angle of attack.

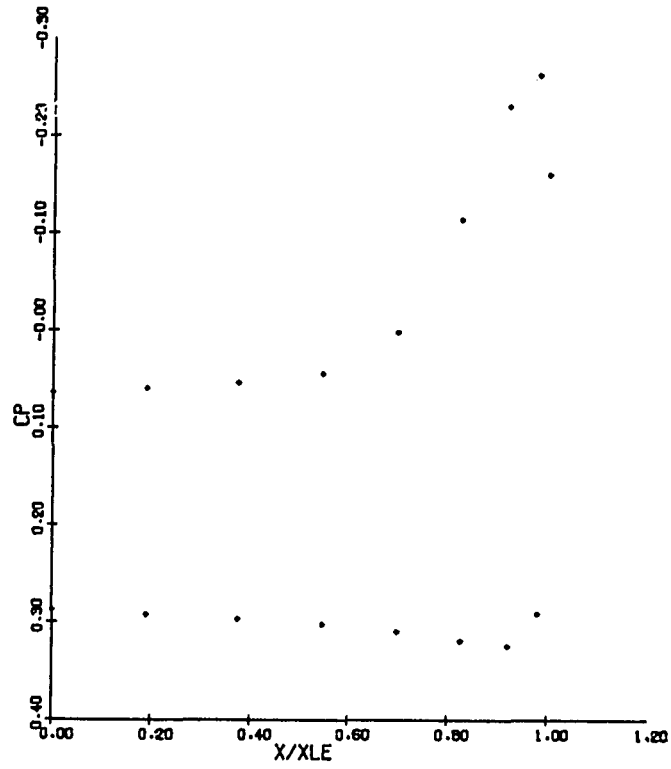


Figure 13b. Surface pressure distribution for a 6:1 elliptic cone at 10° angle of attack with $M_\infty = 1.97$ obtained with the 16 x 16 mesh.

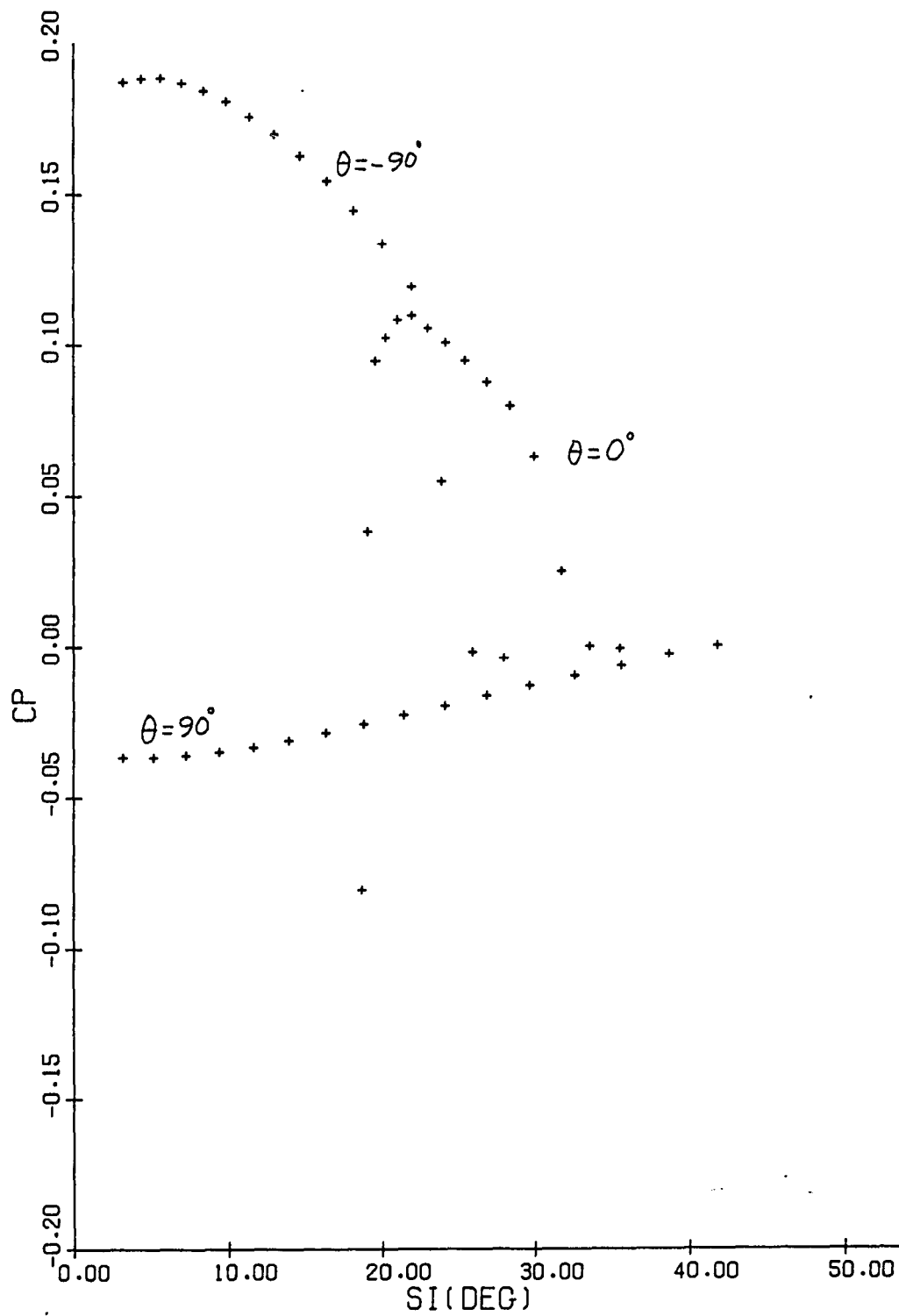


Figure 13c. Pressure variation between the body and the bow shock wave for 6:1 elliptic cone obtained with 16 x 16 mesh.

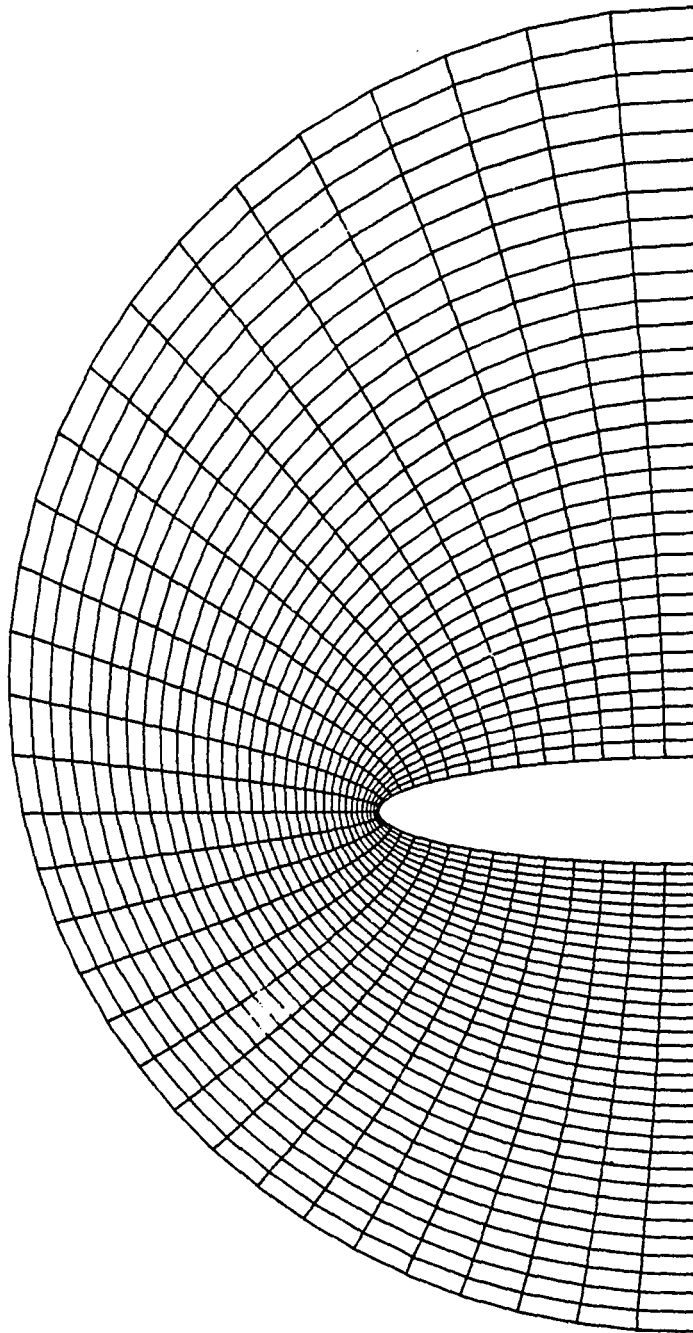


Figure 14a. The 32 x 32 mesh for a 6:1 elliptic cone at 10° angle of attack.

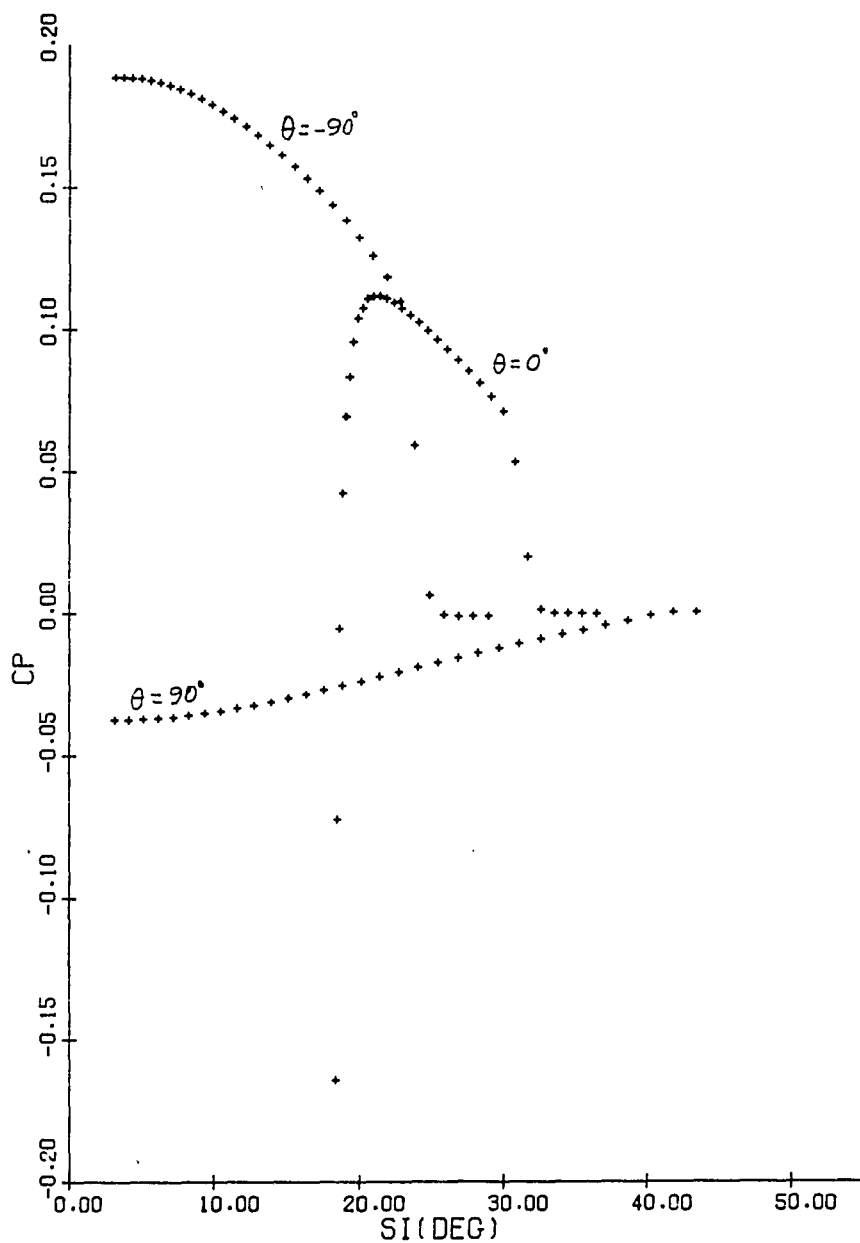


Figure 14b. Pressure variation between the body and the bow shock wave for a 6:1 elliptic cone at 10° angle of attack with $M_\infty = 1.97$ obtained with the 32 x 32 mesh.

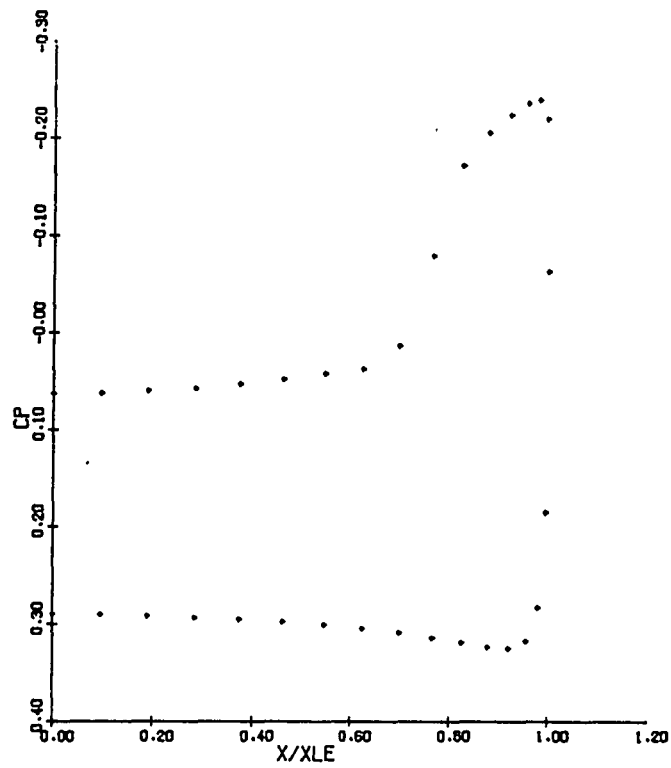


Figure 14c. Surface pressure distribution for a 6:1 elliptic cone at 10° angle of attack with $M_\infty = 1.97$ obtained with the 32 x 32 mesh.

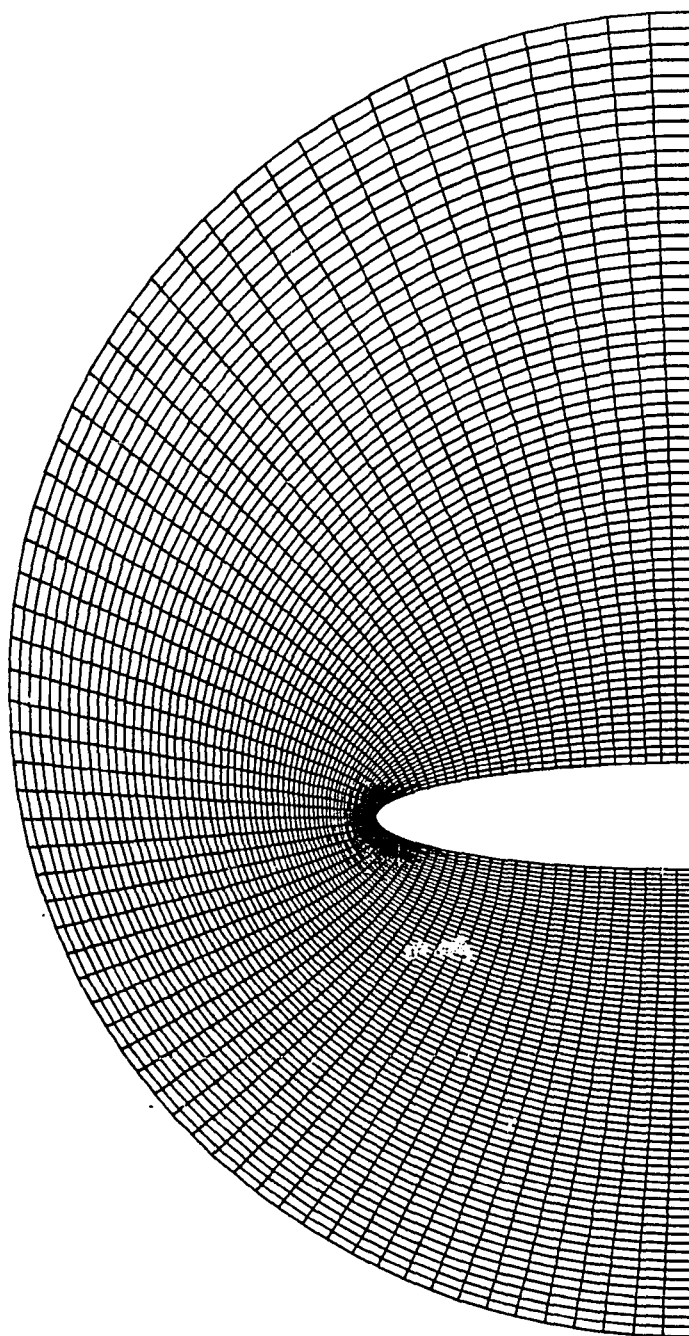


Figure 15a. The 64 x 64 mesh for a 6:1 elliptic cone at 10° angle of attack.

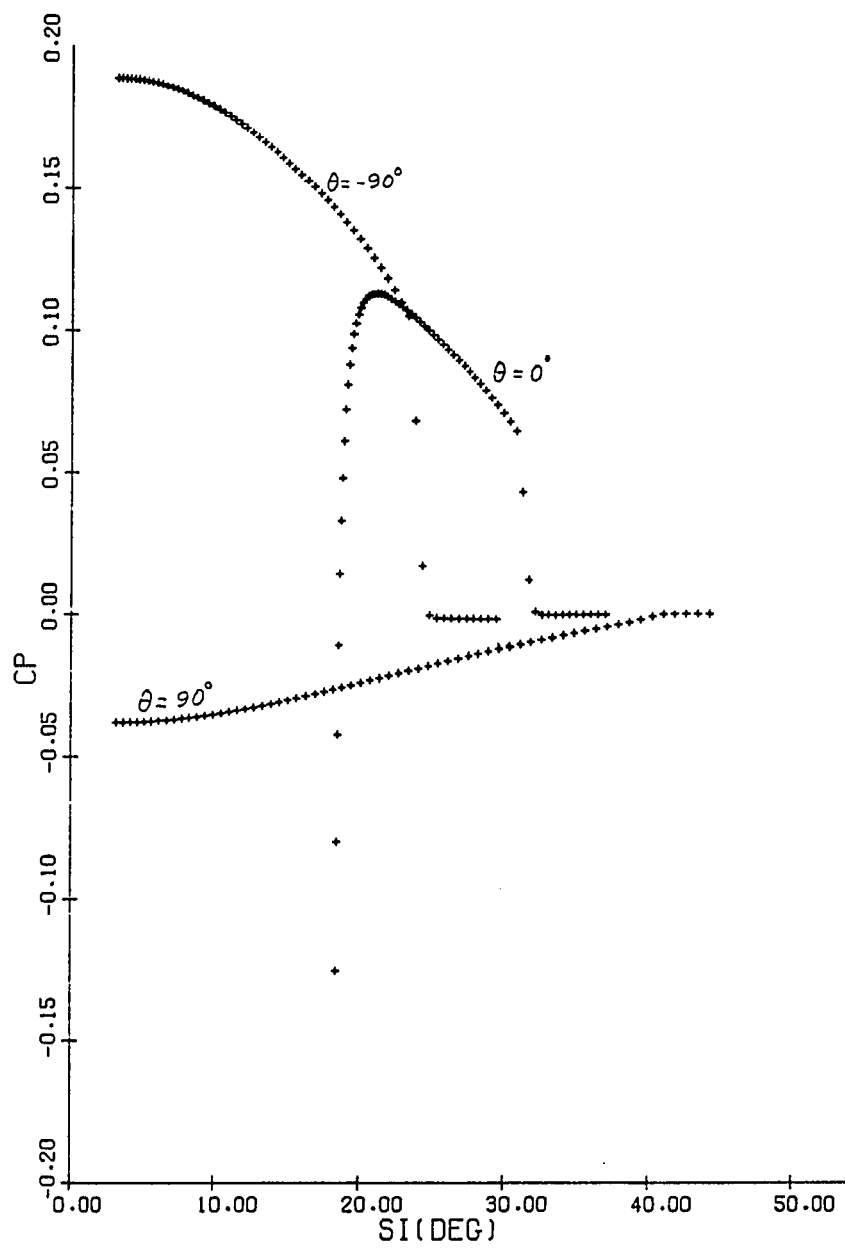


Figure 15b. Pressure variation between the body and the shock wave for the elliptic cone at 10° angle of attack with $M_\infty = 1.97$, obtained with a 64×64 mesh.

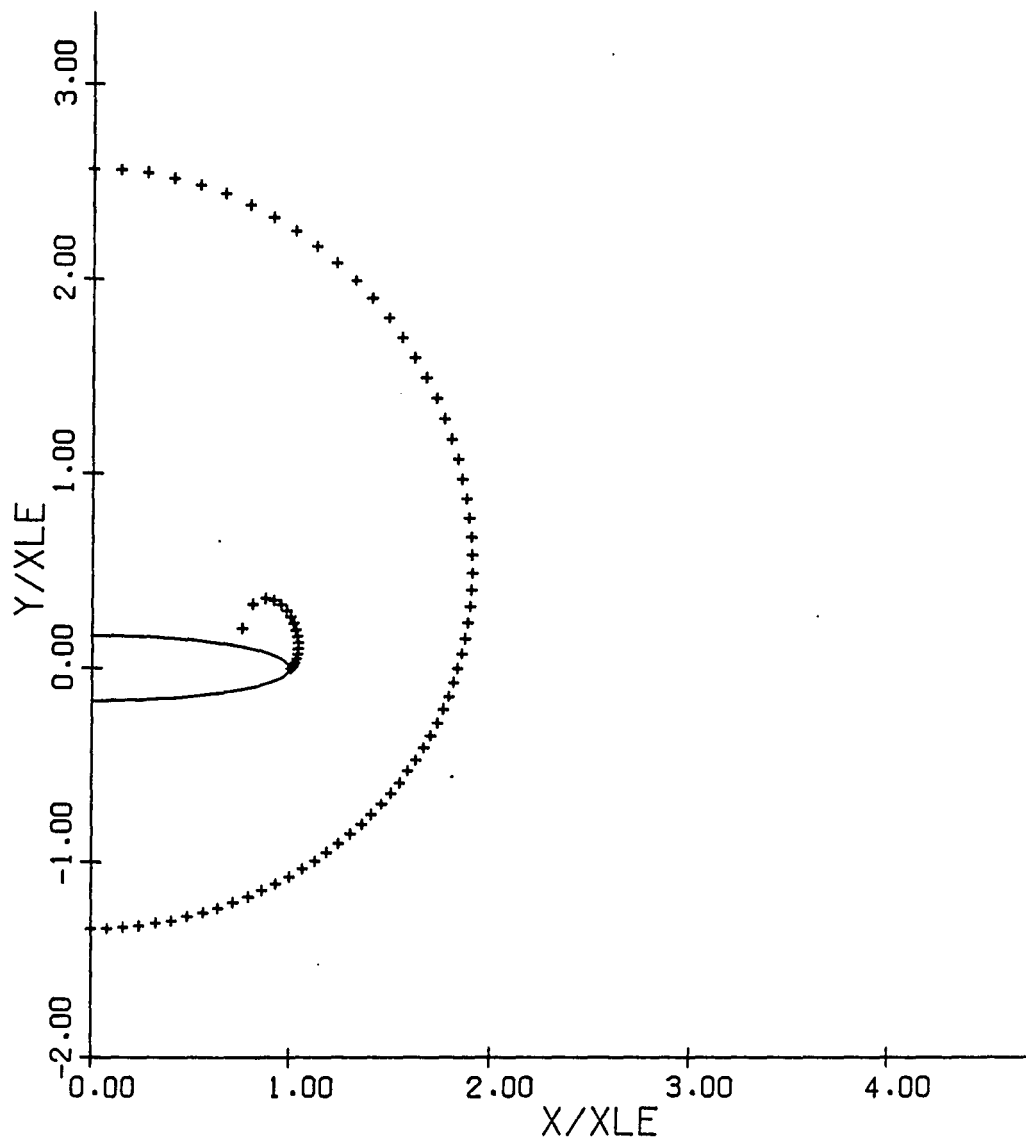


Figure 15c. Bow shock position and the cross-flow sonic surface for the 6:1 elliptic cone at 10° angle of attack with $M_\infty = 1.97$ obtained with a 64 x 64 mesh.

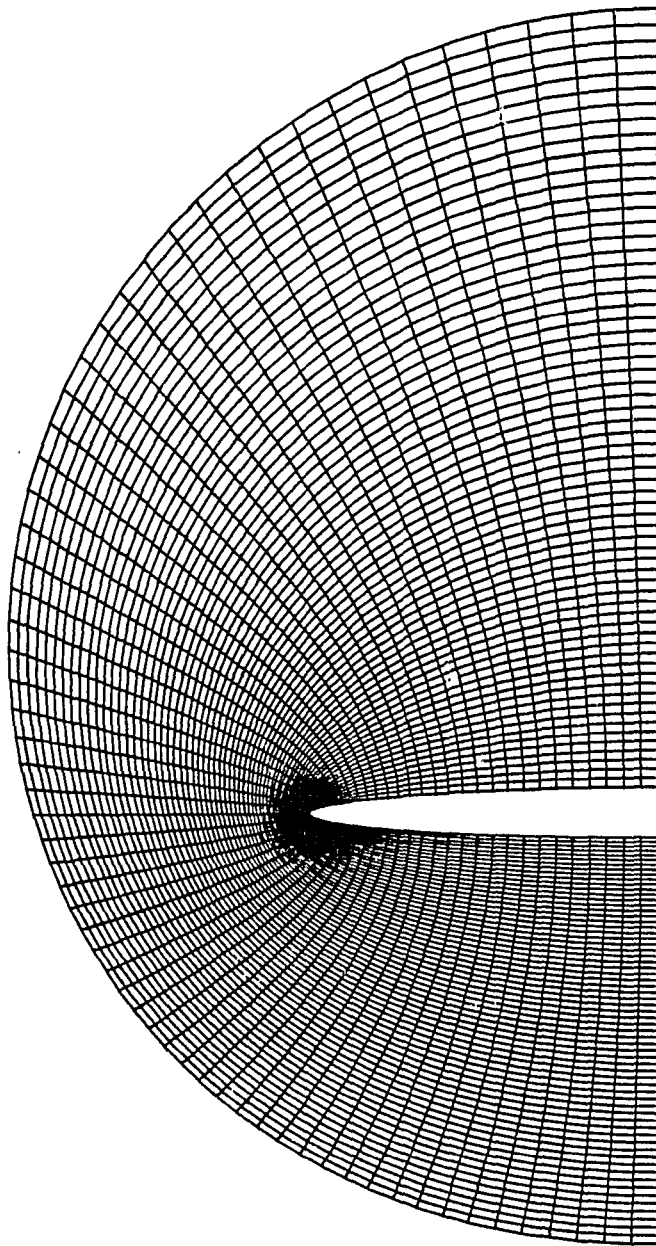


Figure 16a. The 64 x 64 mesh for a 13:1 elliptic cone at 10° angle of attack.

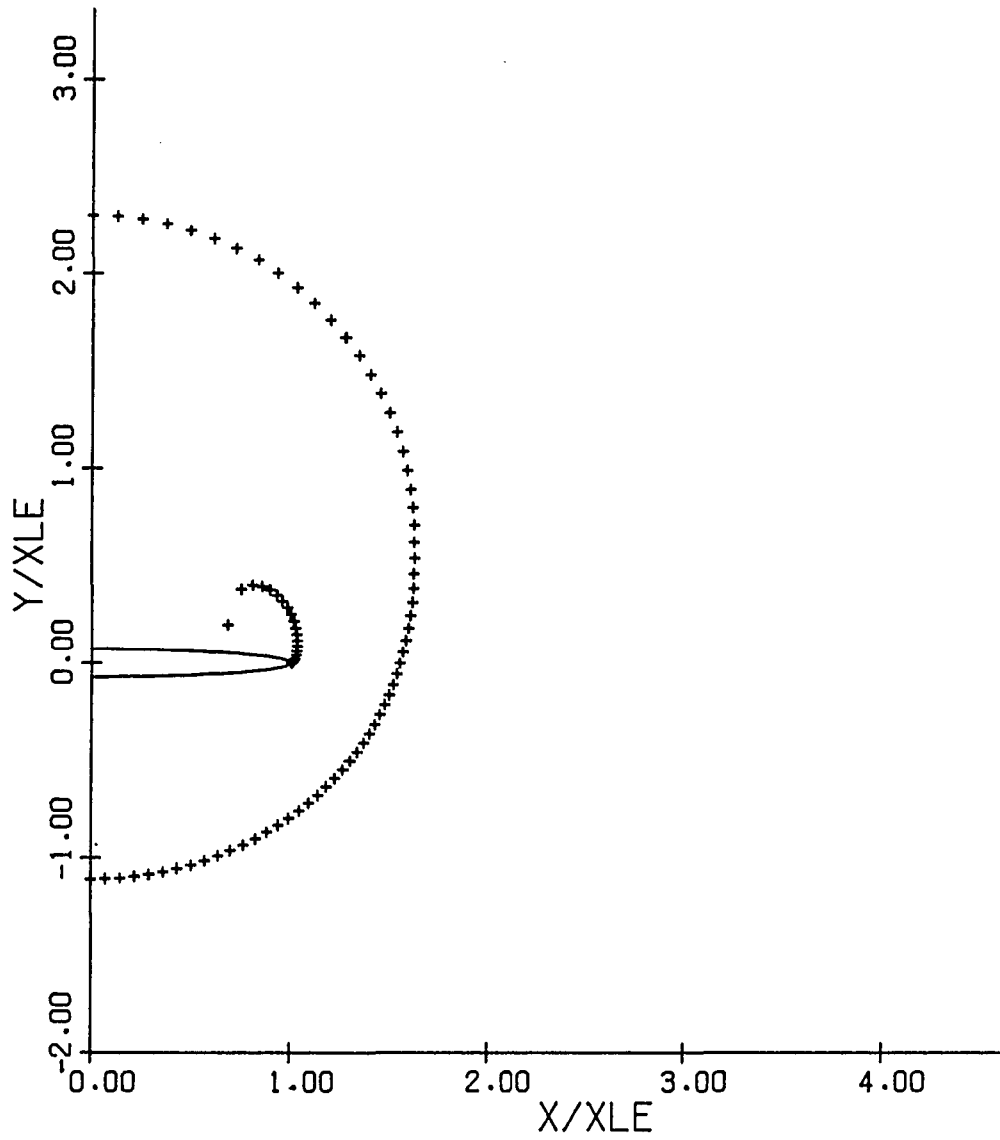


Figure 16b. Bow shock position and the cross-flow sonic surface for a 13:1 elliptic cone at 10° angle of attack.

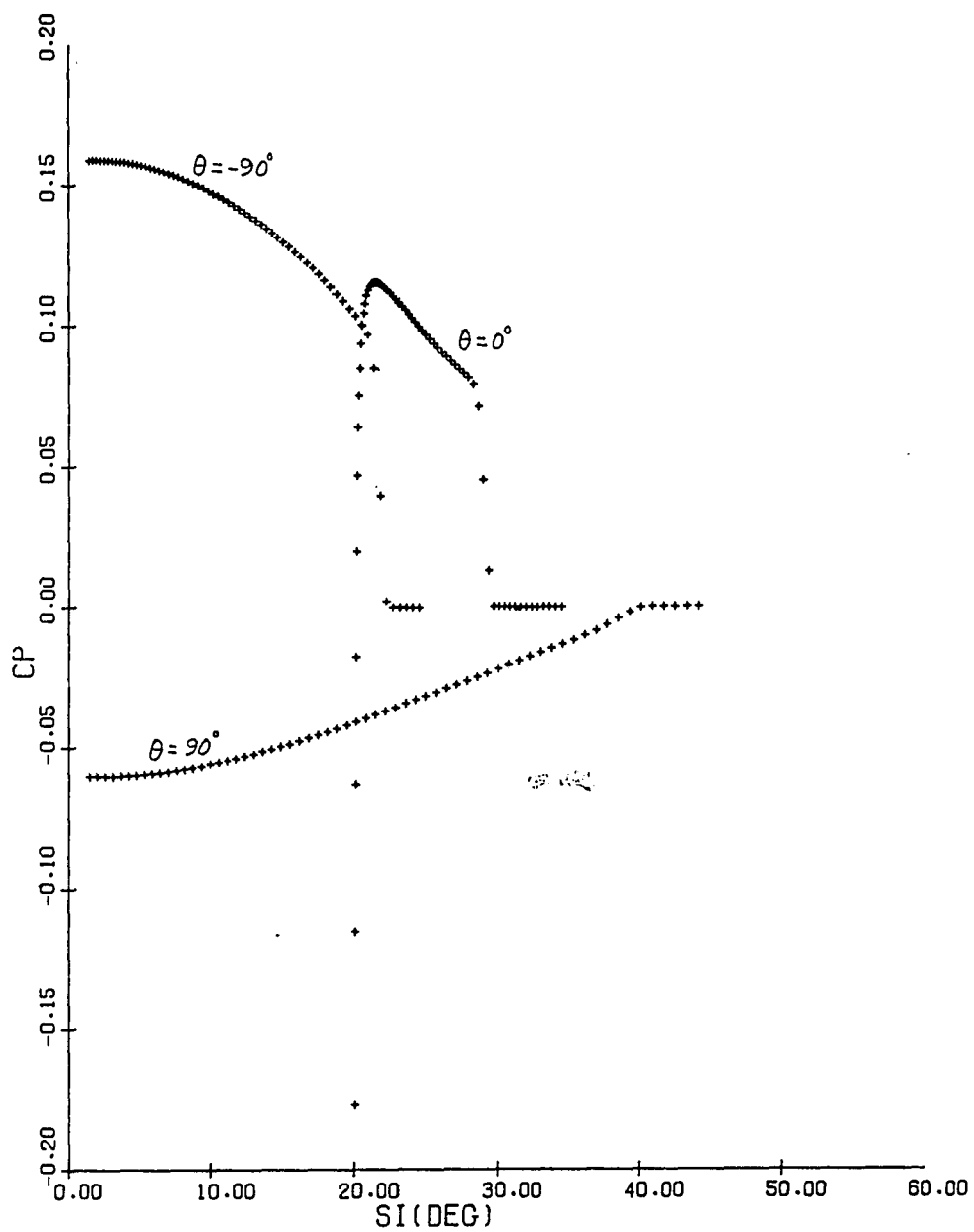


Figure 16c. Pressure variation between the bow shock wave and the body for a 13:1 elliptic cone at 10° angle of attack at $M_\infty = 2.0$.

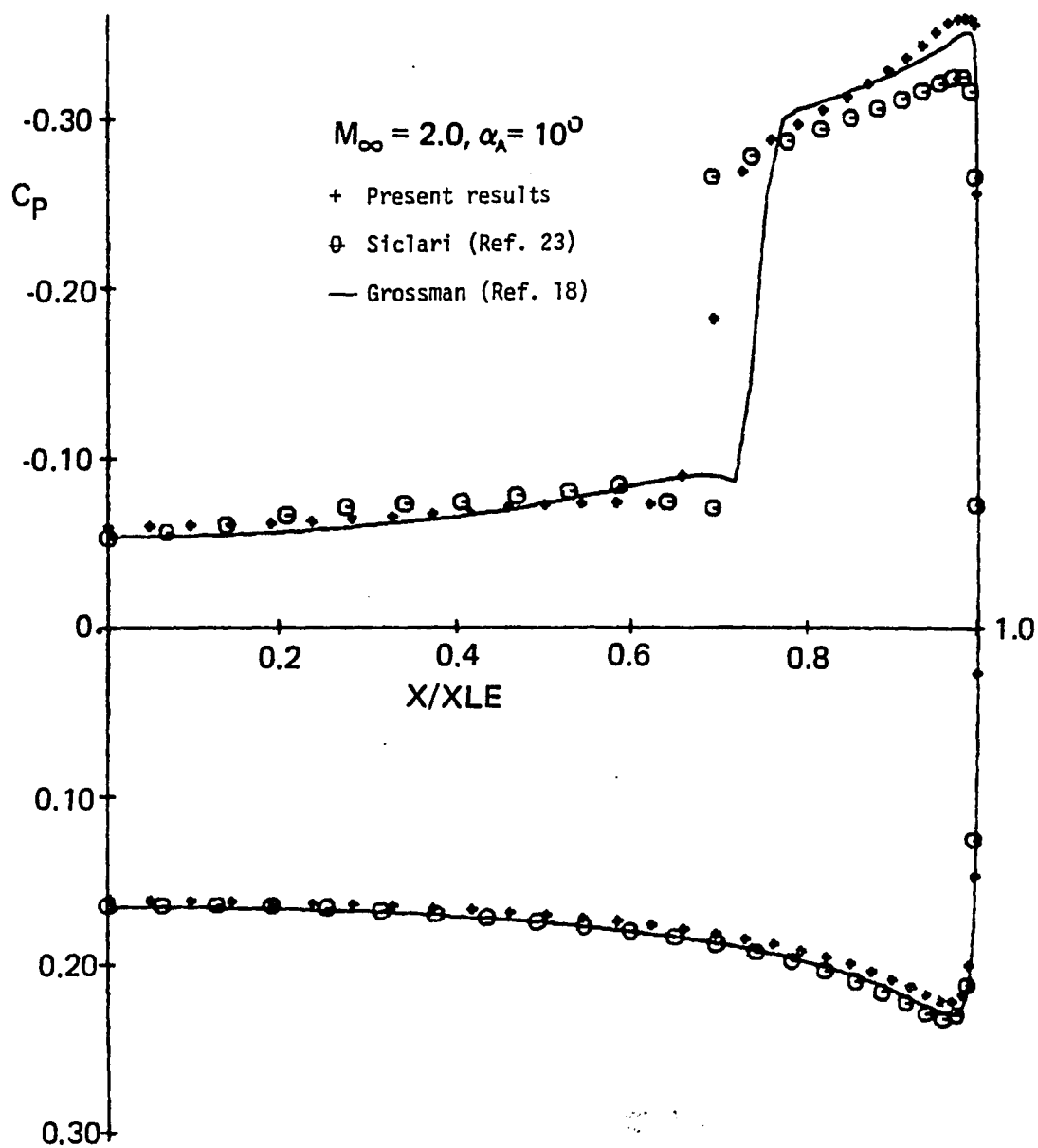


Figure 16d. Comparison of the surface pressure using the Euler equation due to Siclari²³ and a quasilinear formulation of the potential equation due to Grossman¹⁸ with the present result for a 13:1 elliptic cone at 10° angle of attack with $M_\infty = 2.0$

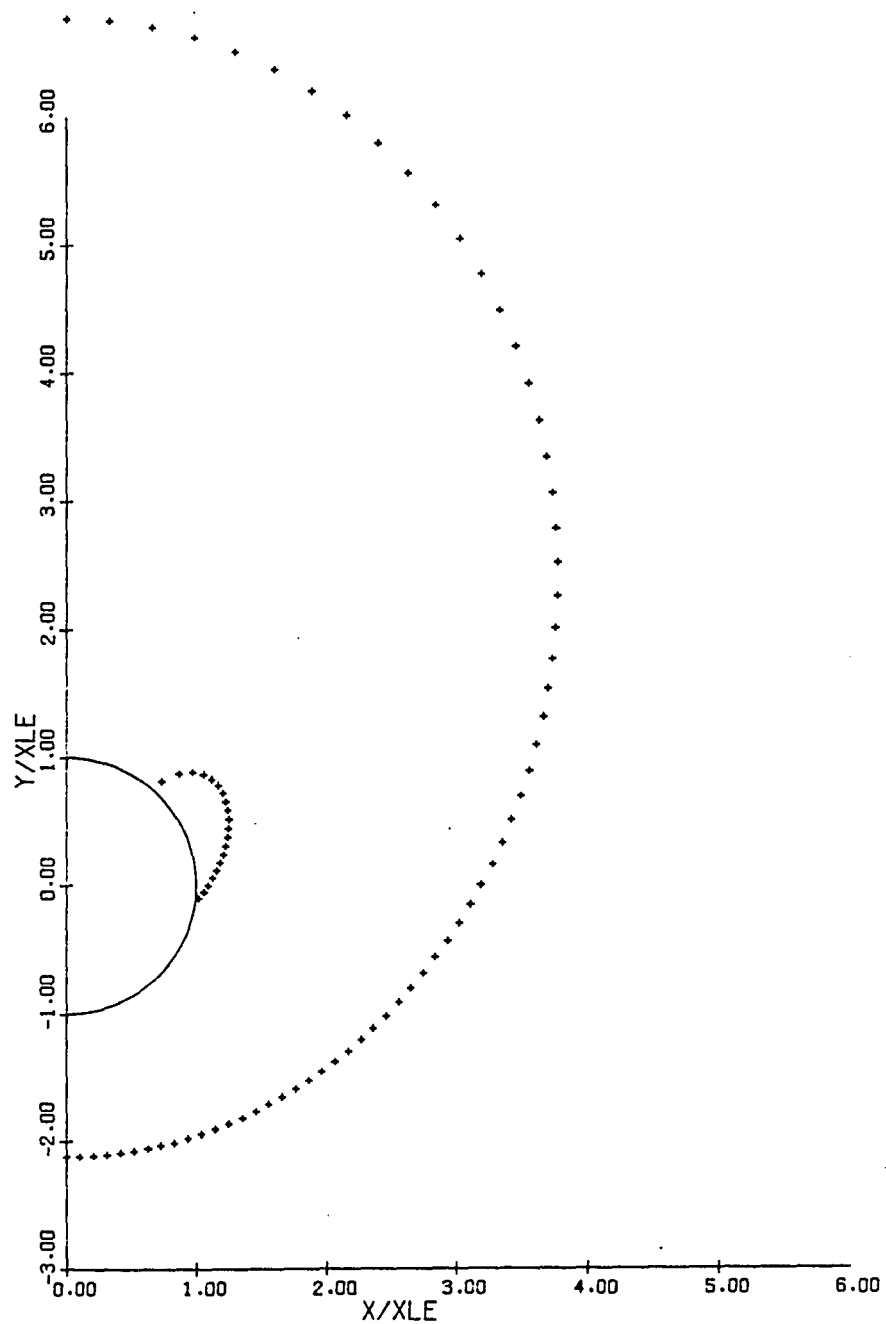


Figure 17a. Bow shock position and the cross-flow sonic surface for a 10° circular cone at 20° angle of attack with $M_\infty = 2$.

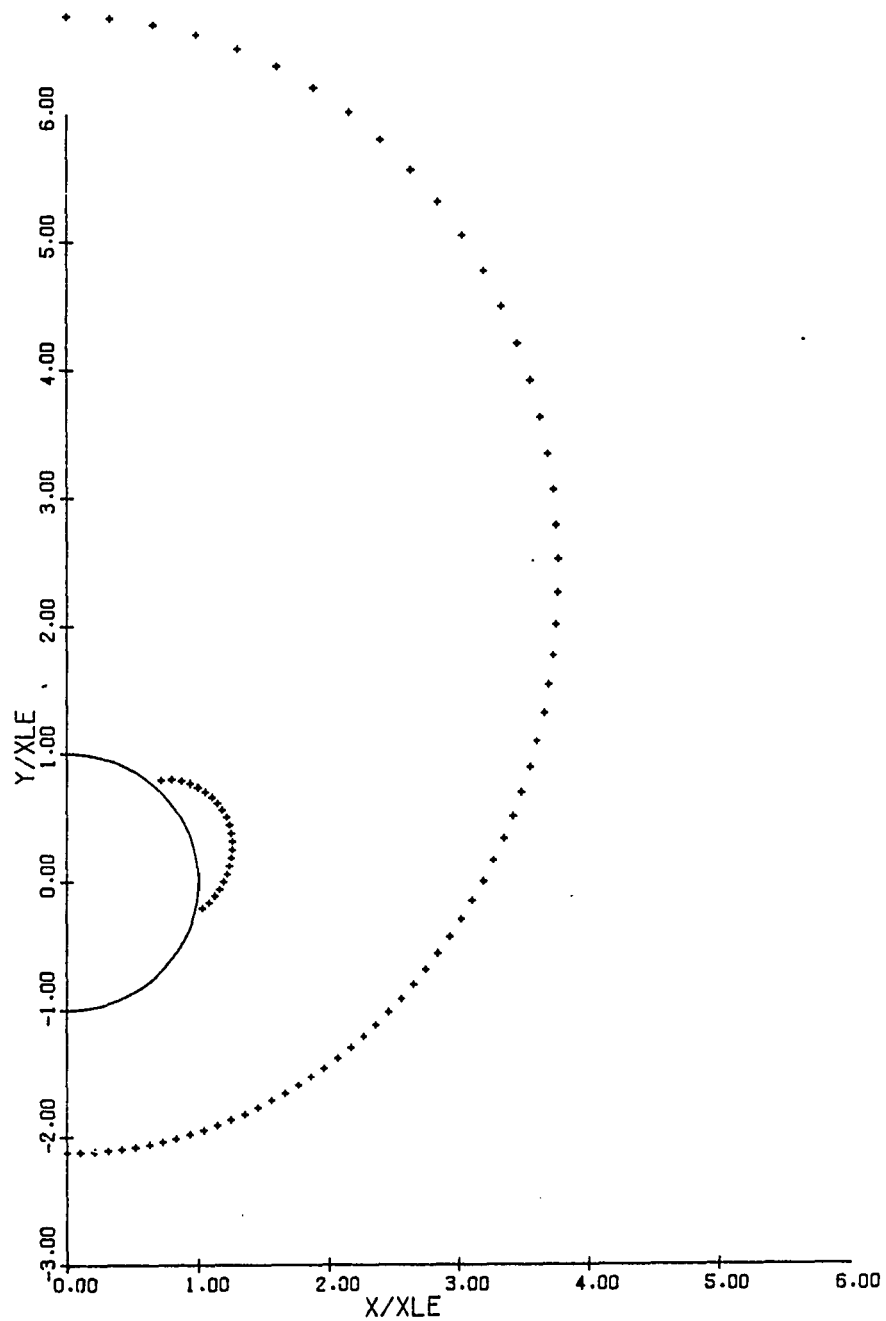


Figure 17b. Bow shock position and the smooth sonic surface obtained by changing the gas law inside the sonic bubble for a 10° circular cone at 20° angle of attack with $M_\infty = 2.0$.

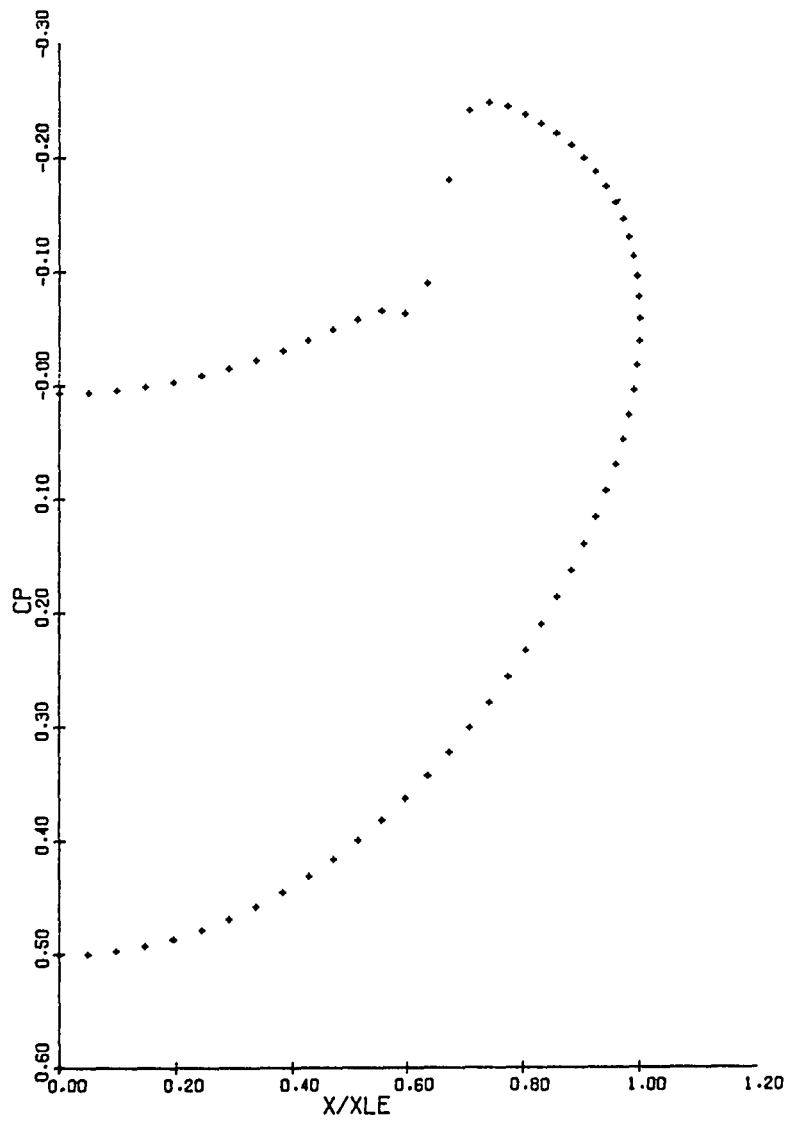


Figure 17c. Surface pressure distribution of a 10° circular cone at 20° angle of attack with $M_\infty = 2.0$.

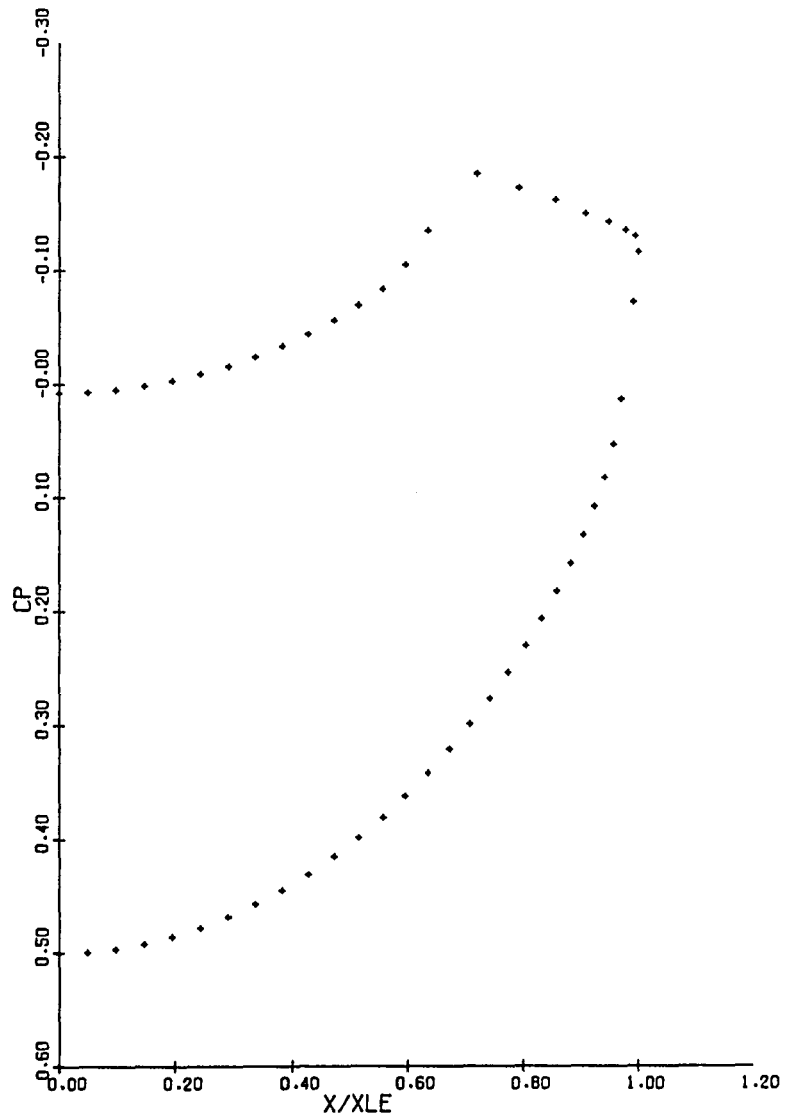


Figure 17d. Surface pressure distribution on the circular cone modified to provide a shock-free cross-flow.

CHAPTER 6

CONCLUSION

An efficient numerical method has been developed for the computation of supersonic conical flows under the potential approximation. This method combines ideas from finite element and finite difference methods in order to solve a quasilinear partial differential equation of mixed type in an arbitrary domain. The type-dependent differencing invoked for the flow field computations was originally developed for planar transonic flows with embedded regions of supersonic flow. Not surprisingly, this differencing also proved to be reliable for conical fields with their extensive supersonic zones and embedded shock waves. The finite area concept is, of course, a general one and could be applied to any vector field on a curved surface described by similar partial differential equations. The conservative differencing implemented here provides a good approximation to the shock locations and shock strengths for flows where the potential approximation is a reasonable one.

Possible improvements to the numerical scheme developed here include the following: instead of capturing the shock waves they could be found through a second-order accurate shock-fitting procedure consistent with the finite area concept; multigrid methods could be used to accelerate the convergence of the iterative procedure;

finally, a higher-order integration method would improve the accuracy of the discretization procedure.

Using this algorithm and the fictitious gas concept, we have also demonstrated that shock-free cross flows are possible for configurations that satisfy a geometric constraint. Two possible extensions of this shock-free design capability could be valuable. First, a generalization of the method of constructing the sonic surface so that it is more likely that no limit lines will be encountered in the Cauchy problem would make the algorithm a better design tool. Second, mathematical analysis is needed to determine whether or not the perturbation problem for flows without cross-flow shocks is properly set. If this is the case, then for conical flows, shock-free cross flows need not be mathematically isolated, as they are in planar flows.

REFERENCES

1. Hayes, W.D. and Probstein, R.F., Hypersonic Flow Theory, Vol. 1, Academic Press, pp. 529-536, 1966.
2. Smith, J.H.B., "Remarks on the Structure of Conical Flows," Progress in Aerospace Sciences, Vol. 12, Pergamon Press, 1972, pp. 241-272.
3. Steger, J.L. and Baldwin, B.S., "Shock Waves and Drag in the Numerical Calculations of Compressible, Irrotational Transonic Flow", AIAA Journal, Vol. 11, No. 17, July 1973, pp. 903-904.
4. Poisson-Quinton, "Slender Wings for Civil and Military Aircraft," ISRAEL Journal of Technology, Vol. 16, 1978, pp. 97-131.
5. Mason, W.H. and Miller, D.S., "Controlled Supercritical Cross Flow on Supersonic Wings - An experimental Validation," AIAA 13th Fluid and Plasma Dynamic Conference, Snowmass, CO, Paper No. 80-1421, July 14-16, 1980.
6. Landrum, E.J. and Miller, D.S., "Assessment of Analytical Methods for the Prediction of Supersonic Flow over Bodies," AIAA Journal, Vol. 19, No. 2, February 1981, pp. 160-164.
7. Sritharan, S.S. and Seebass, A.R., "A Finite Area Method for Nonlinear Conical Flows," AIAA/ASME 3rd Joint Thermophysics, Fluids, Plasma and Heat Transfer Conference, St. Louis, MO, Paper No. 82-0995, June 7-11, 1982.
8. Jameson, A. and Caughey, D.A., "A finite Volume Method for Transonic Potential Flow Calculations," Proceedings of AIAA 3rd Computational Fluid Dynamics Conference, Albuquerque, NM, June 27-29, 1977, pp. 35-54.
9. Lovelock, D. and Rund, H., Tensors, Differential Forms and Variational Principles, John Wiley & Sons, Inc., 1975.
10. Nikolskii, A.A. and Taganov, G.I., "Gas Motion in a Local Supersonic Region and Conditions of Potential-Flow Breakdown," N.A.C.A. Technical Memorandum, No. 1213, May, 1949.
11. Salas, M.D., "Flow Patterns Near a Conical Sonic Line," 17th Aerospace Sciences Meeting, New Orleans, LA, January 15-17, 1979, No. 79-0341.

12. Morawetz, C.S., "The Mathematical Approach to the Sonic Barrier," *Bulletin of The American Mathematical Society*, Vol. 6, No. 2, March 1982, pp. 127-145.
13. Lax, P.D. and Wendroff, B., "Systems of Conservation Law," *Communications on Pure and Applied Mathematics*, Vol. XIII, 1960, pp. 217-237.
14. Rizzi, A.W., "Transonic Solutions of the Euler Equations by the Finite Volume Method," presented at the Symposium Transsonicum II, September 1975.
15. Zienkiewicz, O.C., "Why Finite Elements?", in *Finite Elements in Fluids*, edited by Gallagher, R.H., J.T. Oden, C. Taylor and O.C. Zienkiewicz, Vol. 1, John Wiley & Sons, 1978, pp. 1-23.
16. Jameson, A., "Iterative Solution of Transonic Flows over Airfoils and Wings, Including Flows at Mach 1," *Communications in Pure and Applied Mathematics*, Vol. XXVII, 1974, pp. 283-309.
17. Lax, D., "Hyperbolic Systems of Conservation Laws and the Mathematical Theory of Shock Waves," *SIAM Regional Conference Series in Applied Mathematics* #11.
18. Grossman, B., "Numerical Procedure for the Computation of Irrotational Conical Flows," *AIAA Journal*, Vol. 17, No. 8, August 1979, pp. 828-837.
19. Springer, G., Introduction to Riemann Surfaces, Addison-Wesley, Inc., 1957, pp. 18-24.
20. Thompson, J.F., Thames, F.C. and Mastin, C.W., "Automatic Numerical Generation of Body-Fitted Curvilinear Coordinate System for Field Containing Any Number of Arbitrary Two-Dimensional Bodies," *J. Comp. Phys.*, Vol. 15, 1974, pp. 299-319.
21. Sobieczky, H., Yu, N.J., Fung, K-Y and Seebass, A.R., "New Method for Designing Shock-Free Transonic Configurations," *AIAA Journal*, Vol. 17, No. 7, July 1979, pp. 722-728.
22. Jones, D.J., "Tables of Inviscid Supersonic Flow About Circular Cones at Incidence, $\gamma = 1.4$," *AGARDograph* 137, pt. I, 1969.
23. Siclari, M.J., "Investigations of Crossflow Shocks on Delta Wings in Supersonic Flow," *AIAA Journal*, Vol. 18, No. 1, January 1980, pp. 85-93.